Non-Gaussian noise and data analysis of laser interferometric gravitational wave detectors

(非ガウス雑音とレーザー干渉計型重力波検出器のデータ解析)

理学研究科

数物系専攻

平成 28 年度

Takahiro Yamamoto

(山本尚弘)

Contents

Introduction

Gravitational waves are radiated from the motion of matter and propagate with speed of light in time and space. The existence of gravitational waves are predicted by General theory of relativity[1]. There is an indirect evidence of the existence of gravitational waves. Halse and Taylor detected the decrease of orbital period in the binary pulsar system PSR1913+16, and the measured decreasing rate is consistent with theoretical calculations of GW radiation[2, 3]. The decrease of orbital period is due to the loss of energy by emitting gravitational waves.

The Laser Interferometer Gravitational-Wave Observatory (LIGO)[4] and Virgo[5] collaborations have set many upper limits on GW amplitudes or event rates of various GW sources[6, 7, 8, 9, 10] as they improve the sensitivity of detectors[11, 12]. In 2015, the advanced LIGO[13] (aLIGO) detected one of sources, GW from a binary black hole merger[14, 15] in the first observation run.

The 1st science run(O1) of aLIGO has been taken place and aLIGO is being upgraded their sensitivity toward to the 2nd science run(O2). The Virgo is

also being upgraded to the advanced Virgo (AdVirgo)[16] to improve its sensitivity and the Japanese gravitational wave detector, KAGRA[17], has been constructed and the 1st run has been taken place as initial KAGRA (iKAGRA) observation. At present the KAGRA is being upgraded to bKAGRA to improve its sensitivity. KAGRA will install cryogenic mirrors whose contributions for improving the sensitivity for gravitational wave was verified by the CLIO[18, 19] which is a proto-type detector of KAGRA.

In the next decade, many gravitational wave events are expected to be detected with world wide network of GW detectors. When the gravitational wave events with low signal-to-noise ratio are detected, the understanding of the detector noise behavior becomes more important. In many previous works, the reduction of false noise events and the improvement of the estimation of the noise behavior such as the power spectrum of the detector noise are done by identifying non-stationary noises and their sources. Evaluation of the non-Gaussianity in addition to the non-stationarity can provides new information on the detector noise behavior. Moreover the indicator of non-Gaussianity may help to improve the GW search method which is optimal for the Gaussian background, when the detector noise distribution deviates from stationary Gaussian distribution. In many previous works, the stationary non-Gaussian noise is not distinguished from non-stationary noise in explicitly though the various noise models were suggested for gravitational wave searches. Although [50] focused on stationary non-Gaussian noise using the Student-t noise model and a pa-

rameter ν of the Student-t distribution as an indicator of the non-Gaussianity, the statistical character of ν was not discussed enough for adopting this noise model. This thesis discuss a method to evaluate the non-Gaussianity of the detector noise and to optimize search methods for the non-Gaussian noise using Student-t noise model. We investigate a statistical behavior of the indicator ν in order to adopt the search method assuming Student-t noise model. The outliers of the distribution of the detector noise can be evaluated with the indicator ν which is a parameter of the Student-t noise model. We clarify the confidence interval and threshold of ν above which the Gaussian hypothesis is rejected, and reveal the domination of the non-Gaussian of LIGO observational data statistically. The confidence interval and threshold of ν for the 4096 seconds long data are $15.45 \leq \nu \leq 27.29$ (for $\hat{\nu} = 25$) and $\nu_{\rm th} = 91.4$, respectively. By using this confidence interval and the threshold, we reveal the domination of the non-Gaussianity in the advanced LIGO and iKAGRA observational data and reject the assumption that the detector noise follows Gaussian distribution statistically. The evaluation of ν as an indicator of the non-Gaussianity of detector noise is described in Chapter 3.

In Chapters 4 and 5, to improve the search method for gravitational waves, we adopt likelihood function of the Student-t noise model as an optimal filter instead of the matched filtering method which is used for searching the gravitational waves from compact binary coalescences and is an optimal filter for the Gaussian noise. We show that the GW150914 which is the first

event of the gravitational wave from binary black holes detected by two advanced LIGO can be detected by the likelihood function of the Student-t noise model. This work suggests importance and usefulness to take into account of the non-Gaussianity of the detector noise.

Chapter 1

Detection of Gravitational Wave

1.1 Gravitational Wave

1.1.1 The Einstein's equation

In the Einstein's theory of general relativity, the line element, $\mathrm{d}s$, between different two points is described as

$$\mathrm{d}s^2 = g_{\mu\nu}\mathrm{d}x^\mu \mathrm{d}x^\nu \tag{1.1}$$

where $g_{\mu\nu}$ is the metric tensor. $g_{\mu\nu}$ is determined by Einstein's equation.

The Einstein's equation which expresses the interaction between gravity and masses is described as

$$G_{\mu\nu} = \frac{8\pi G}{c^4} T_{\mu\nu}, \tag{1.2}$$

where $G_{\mu\nu}$ is Einstein's tensor, G is Newton's gravitational constant, c is the speed of light and $T_{\mu\nu}$ is the energy momentum tensor. The Einstein's tensor

is defined as

$$G_{\mu\nu} \equiv R_{\mu\nu} - \frac{1}{2} g_{\mu\nu} R, \tag{1.3}$$

where $R_{\mu\nu}$ and R are called Ricci tensor and Ricci scalar respectively, and are defined as

$$R_{\mu\nu} \equiv \Gamma^{\alpha}_{\mu\nu,\alpha} - \Gamma^{\alpha}_{\mu\alpha,\nu} + \Gamma^{\beta}_{\mu\nu}\Gamma^{\gamma}_{\beta\gamma} + \Gamma^{\beta}_{\mu\gamma}\Gamma^{\gamma}_{\nu\beta}, \tag{1.4}$$

$$R \equiv g^{\mu\nu} R_{\mu\nu}, \tag{1.5}$$

where $\Gamma^{\mu}_{\nu\lambda}$, which is called Christoffel symbol, is defined as

$$\Gamma^{\mu}_{\nu\lambda} \equiv \frac{1}{2} g^{\mu\alpha}(g_{\alpha\nu,\lambda} + g_{\alpha\lambda,\nu} - g_{\nu\lambda,\alpha}). \tag{1.6}$$

1.1.2 Wave equation of space-time

The Einstein's equation is non-linear. The perturbation, $h_{\mu\nu}$ to the flat Minkowski metric $\eta_{\mu\nu}$ is defined as

$$g_{\mu\nu} = \eta_{\mu\nu} + h_{\mu\nu}, \tag{1.7}$$

where $\eta_{\mu\nu}$ is

$$\eta_{\mu\nu} = \begin{pmatrix} -1 & 0 & 0 & 0 \\ 0 & 1 & 0 & 0 \\ 0 & 0 & 1 & 0 \\ 0 & 0 & 1 & 0 \end{pmatrix} \tag{1.8}$$

and $|h_{\mu\nu}| \ll 1$.

In this assumption, Eq. (1.3), (1.4), (1.5) and (1.6) become to the first order of $h_{\mu\nu}$

$$G_{\mu\nu} = \frac{1}{2}h^{,\alpha}_{\alpha\nu,\mu}[h^{,\alpha}_{\alpha\mu,\nu} - h^{,\alpha}_{\mu\nu,\alpha} - h_{,\mu\nu} + \eta_{\mu\nu}(h^{,\alpha\lambda}_{\alpha\lambda} - h^{,\alpha}_{,\alpha})] \tag{1.9}$$

$$R_{\mu\nu} = \frac{1}{2}(h^{,\alpha}_{\alpha\nu,\mu} + h^{,\alpha}_{\alpha\mu,\nu} - h^{,\alpha}_{\mu\nu,\alpha} - h_{,\mu\nu}) \tag{1.10}$$

$$R = h^{,\mu\nu}_{\mu\nu} \tag{1.11}$$

$$\Gamma^{\mu}_{\nu\lambda} = \frac{1}{2}\eta^{\mu\alpha}(h_{\alpha\nu,\lambda} + h_{\alpha\lambda,\nu} - h_{\nu\lambda,\alpha}), \tag{1.12}$$

where h is trace of $h_{\mu\nu}$ defined as

$$h \equiv \eta^{\mu\nu}h_{\mu\nu}. \tag{1.13}$$

We define a tensor

$$\bar{h}_{\mu\nu} = h_{\mu\nu} - \frac{1}{2}\eta_{\mu\nu}h, \tag{1.14}$$

and impose Lorentz gauge condition,

$$\bar{h}^{\mu\nu}_{,\nu} = 0, \tag{1.15}$$

the Einstein's equation can be rewritten as

$$\frac{1}{2}\bar{h}^{,\alpha}_{\mu\nu,\alpha} = -\frac{8\pi G}{c^4}T_{\mu\nu}. \tag{1.16}$$

In the vacuum, $T_{\mu\nu}$ is 0, we have

$$\left(\nabla - \frac{1}{c^2}\frac{\partial^2}{\partial t^2}\right)\bar{h}_{\mu\nu} = 0. \tag{1.17}$$

Eq. (1.17) is the equation expressing the propagation of gravitational wave with speed of light, c, in vacuum.

A plane wave is one of the solution of Eq. (1.17),

$$\bar{h}_{\mu\nu} = A_{\mu\nu} \exp(ik_\rho x^\rho), \tag{1.18}$$

where $A_{\mu\nu}$ is the amplitude of the gravitational wave and k_ρ is the four-wave vector. Two conditions

$$k^\rho k_\rho = 0 \tag{1.19}$$

and

$$A_{\mu\rho} k^\rho = 0 \tag{1.20}$$

are needed for Eq. (1.18) to satisfy Eq. (1.15) and (1.17). Eq. (1.20) expresses that gravitational waves are transverse waves. An arbitrariness of the choice of coordinates remains even though Lorentz gauge condition is imposed. We can impose the traceless condition,

$$A^\alpha_\alpha = 0, \tag{1.21}$$

and the transverse condition,

$$A_{\alpha\beta} U^\beta = 0, \tag{1.22}$$

where U_β is an unit vector of time. Eq. (1.20), (1.21) and (1.22) are called the Transverse-Traceless (TT) gauge. In these conditions, the gravitational wave

which propagates in direction of z-axis can be described as

$$\bar{h}_{\mu\nu} = A_{\mu\nu} \mathrm{e}^{ik(ct-z)}, \tag{1.23}$$

$$A_{\mu\nu} = \begin{pmatrix} 0 & 0 & 0 & 0 \\ 0 & A_{12} & A_{13} & 0 \\ 0 & A_{13} & -A_{12} & 0 \\ 0 & 0 & 0 & 0 \end{pmatrix} = \begin{pmatrix} 0 & 0 & 0 & 0 \\ 0 & h_+ & h_\times & 0 \\ 0 & h_\times & -h_+ & 0 \\ 0 & 0 & 0 & 0 \end{pmatrix}, \tag{1.24}$$

where h_+ and $h_\times$ are the polarization of the gravitational waves and are shown in FIG. 1.1.

1.1.3 Gravitational wave radiation

We consider the radiation of the gravitational wave from a object whose velocity is much smaller than the speed of light. In this case, the linear approximation can be used. The Einstein's equation can be written as

$$\left(\nabla - \frac{1}{c^2} \frac{\partial^2}{\partial t^2} \right) \bar{h}^{\mu\nu} = \frac{16\pi G}{c^4} \tau^{\mu\nu}, \tag{1.25}$$

where $\tau^{\mu\nu}$ is the energy momentum tensor. Eq. (1.25) can be solved by using a Green's function which is the same as the radiation of electromagnetic wave. $\bar{h}^{\mu\nu}$ is given as

$$\bar{h}^{\mu\nu}(x) = -\frac{4G}{c^4} \int \frac{\tau^{\mu\nu}(x'_i, x^0 - |x_i - x'_i|)}{|x_i - x'_i|} \mathrm{d}^3 x', \tag{1.26}$$

where x'_μ is mass distribution of the matter and x_μ is the observation point which is far enough away from the matter, and i is 1, 2, or 3.

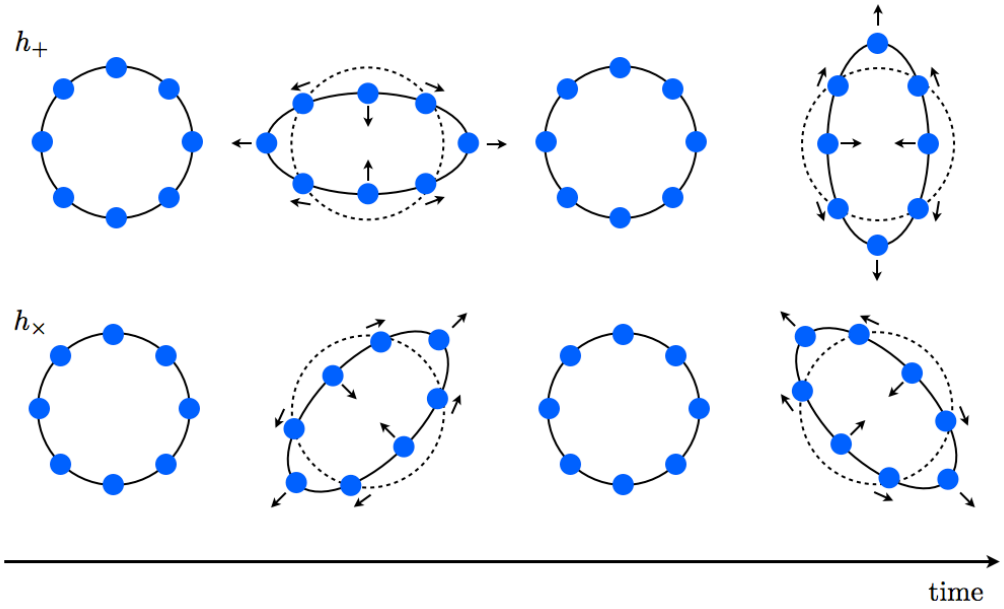

Figure 1.1: The time evolution of the two polarization, h_+ and $h_\times$, of a gravitational wave in the case when the gravitational wave enters vertical direction to the sheet. The blue filled circles represent free masses.

When the Eq. (1.26) is expanded around the center of gravity of the matter, $x^0_G = x^0 - |x_i - x'_i|$, by using multipole expansion, the following results are obtained,

$$\bar{h}^{00} = -\frac{4G}{c^4 r}\left[\int \tau^{00}(x'_i, x^0_G)\mathrm{d}^3x' + \frac{x_l}{r}\frac{\partial}{\partial x^0_G}\int x'^l \tau^{00}(x'_i, x^0_G)\mathrm{d}^3x' + \cdots\right], \quad (1.27)$$

$$\bar{h}^{0k} = -\frac{4G}{c^4 r}\left[\frac{\partial}{\partial x^0_G}\int x'^k \tau_{00}(x'_i, x^0_G)\mathrm{d}^3x' + \frac{1}{2}\frac{x_l}{r}\frac{\partial}{\partial x^0_G}\frac{\partial}{\partial x^0_G}\int x'^l x'^k \tau^{00}(x'_i, x^0_G)\mathrm{d}^3x' + \cdots\right], \quad (1.28)$$

$$\bar{h}^{lk} = -\frac{2G}{c^4 r}\left[\frac{\partial}{\partial x^0_G}\frac{\partial}{\partial x^0_G}\int x'^l x'^k \tau^{00}(x'_i, x^0_G)\mathrm{d}^3x' + \cdots\right], \quad (1.29)$$

where $r = |x_i - x_{G,i}|$. The first term of the Eq. (1.27) represents Newton's gravitational field. The first term of the Eq. (1.28) represents the dipole radiation. However there are no dipole radiation of the gravitational wave because at the center of mass frame, $\int \rho x^i \mathrm{d}^3x$ equal zero, where ρ is the mass density. The first term of the Eq. (1.29) represents quadrupole radiation at the lowest-order of gravitational radiation.

The dimension of the first term of the quadrupole radiation is energy. When we replace this term with the kinetic energy of the gravitational wave source, the amplitude of the gravitational wave can be described as

$$\bar{h}^{lk} \sim \frac{2G}{rc^4} M v^4, \quad (1.30)$$

where M and v are the mass and the speed of motion of the gravitational wave source.

1.2 Gravitational Wave Sources

1.2.1 Compact binary Coalescence

The first event which is named GW150914 detected by aLIGO is a coalescence of binary black holes. Binary coalescence event has been regarded as one of the most strong source of GWs.

Binary systems emit gravitational radiation. Then the orbital radius shrinks with time and the frequency of emitted GWs increases until the coalescence.

The frequency of GWs when a binary system coalesces can be written in approximately as

$$f_{\mathrm{ISCO}} \simeq 2.2\mathrm{kHz} \left(\frac{M_\odot}{m} \right) \tag{1.31}$$

where $M_\odot$ is the mass of the Sun and m is the total mass of the binary system[20].

Although the lifetime of the these systems is millions of years, GW signals can be detected only a few minutes before the coalescence in the case of binary neutron stars because the ground-based interferometric GW detectors can detect GWs whose frequency is above 10Hz.

The matched filtering technique is often used for searching GWs from binary systems, because the GW waveform from these systems can be calculated accurately by using the post-Newtonian approximation of general relativity when the distance between the two objects is enough large.

FIG. 1.2 shows the theoretical gravitational wave waveform from compact

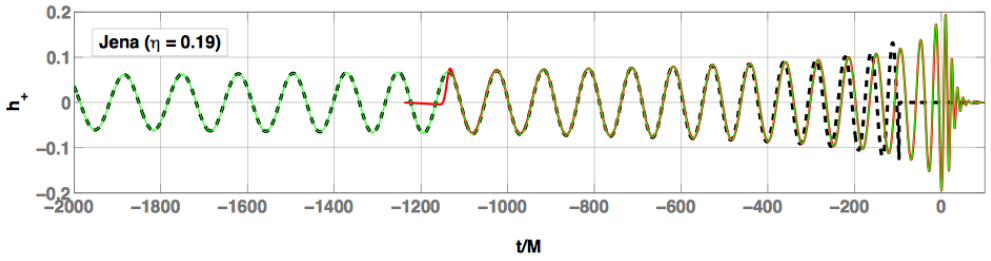

Figure 1.2: This plot shows the theoretical gravitational wave waveform from compact binary systems[21].

binary systems[21]. The amplitude and frequency of the gravitational wave increase with time until merger of two stars.

In matched filtering technique, we prepare the theoretical waveform such as FIG.1.2 for various masses and adopt these waveforms as the template.

The total mass and the frequency for the binary black hole coalesces of GW150914 are $m = 70.4M_\odot$ and $f_{\rm ISCO} = 64.3$, respectively.

1.2.2 Supernova

GWs are expected to be emitted with supernova explosions. Though it is difficult to predict the theoretical waveform from this kind of source, the typical frequency of GWs and the duration of signals are expected to be around 1kHz and a few hundred mili-seconds, respectively. The expected amplitude is [22]

$$h \sim 2.7 \times 10^{-20} \left(\frac{\Delta E}{M_\odot c^2}\right)^{1/2} \left(\frac{1\text{kHz}}{f}\right)^{1/2} \left(\frac{10\text{Mpc}}{r}\right), \tag{1.32}$$

where ΔE is the amount of the emitted energy. The expected value of the order of $\Delta E/(M_\odot c^2)$ is around 10^{-6}.

1.2.3 Pulsar

The pulsar is the astronomical object rotating and emitting pulsed electromagnetic wave. Its period of the rotation is from a few mili-seconds to a few seconds. A spinning neutron star which has the asymmetry in the inertia moment can also emit GWs whose frequencies are twice of the frequency of the rotation. The amplitude of GWs can be estimated as

$$h \sim 3 \times 10^{-27} \left(\frac{10 \text{ kpc}}{r} \right) \left(\frac{f}{200 \text{ Hz}} \right)^2 \left(\frac{\epsilon}{10^{-6}} \right) \tag{1.33}$$

where ϵ is the asymmetry in the inertia moment. The amplitude of GWs from this source is expected to be weaker than one from the compact binary coalescence and the supernova explosions. However the spinning neutron stars can emit GWs continuously so we can improve the signal-to-noise ratio by integrating the signal for a long period.

Many pulsars are known by electromagnetic observation and are set upper limits by gravitational wave searches. Some upper limits for the gravitational wave amplitude from pulsar by LIGO and Virgo collaboration are shown in Table 1.1[23].

1.3 Data analysis method of the various sources

There are two types of gravitational wave. In one case, the waveform is known theoretically like binary coalescences, and in the other case, the waveform is unknown like supernova explosions.

Table 1.1: The upper limit for the gravitational wave amplitude from well known pulsars[23].

Source	frequency [Hz]	$h_{\text{upper limit}}$
Vela	22.3840	3.2×10^{-24}
Crab	59.4448	7.0×10^{-25}

Matched filtering method

When the waveform we want to search is known, the matched filter is one of the most efficient method. The inputs of matched filter are the detector signal s and the template waveform h_T. The matched filter is expressed as

$$\rho = \int_{-\infty}^{\infty} \frac{s(f)h_T^*(f)}{S_{\rm n}(f)} {\rm d}f, \tag{1.34}$$

where ρ is detection statistic of the matched filter and $S_{\rm n}(f)$ is the power spectrum density of the detector noise. The basic idea of this method is to compute the inner product between the gravitational wave signal and template waveform. The inner product is weighted by the detector sensitivity, $S_n(f)$. When we assume that the detector signal, s, contains the gravitational wave signal, h and the noise, n, the detection statistic, ρ can be rewritten as

$$\rho = \int_{-\infty}^{\infty} \frac{h(f)h_T^*(f)}{S_{\rm n}(f)} {\rm d}f + \int_{-\infty}^{\infty} \frac{n(f)h_T^*(f)}{S_{\rm n}(f)} {\rm d}f. \tag{1.35}$$

From Eq. (1.35), the statistical behavior of ρ depends on one of the noise.

Excess power method

When the waveform of gravitational wave is difficult to know theoretically, the excess power method is one of the efficient method[24, 25]. The excess power method can be described as

$$\begin{aligned} \epsilon &= \int_{-\infty}^{\infty} \frac{s(f)s^*(f)}{S_{\rm n}(f)}{\rm d}f \\ &= \int_{-\infty}^{\infty} \frac{h(f)h^*(f)}{S_{\rm n}(f)}{\rm d}f + 2\int_{-\infty}^{\infty} \frac{h(f)n^*(f)}{S_{\rm n}(f)}{\rm d}f + \int_{-\infty}^{\infty} \frac{n(f)n^*(f)}{S_{\rm n}(f)}{\rm d}f, \end{aligned} \tag{1.36}$$

The statistical behavior of detection statistic, ϵ, also depends on n.

In order to understand the statistical behavior of the detection statistics of both method we should investigate the noise distribution. The precision of the expected value of the noise power spectrum, $S_{\rm n}(f)$, depends on the standard deviation of the noise because we should estimate $S_{\rm n}(f)$ from the finite length data in general. Statistical behavior of the detection statistics can be described easy when the detector noise is Gaussian. The Gaussianity of the detector noise is described in Chapter 2.

1.4 Laser Interferometric Gravitational Wave Detector

1.4.1 Principle of Interferometric Detectors

Michelson interferometers operate as the gravitational wave detectors. A simple Michelson interferometer consists of laser, beam splitter, two mirrors, and photodetector. Figure 1.3 shows the simple Michelson interferometer. Laser light is separated into two arms of the interferometer at the beam splitter, and reflected at the mirrors which are suspended at the end of the two arms. Reflected light comes back to beam splitter, and the photodetector receives interference of the light from two arms. Because two suspended mirrors correspond to free masses, incident gravitational waves toward interferometer change the optical path length of the two arms. Gravitational waves can be detected as a change of the intensity of the interference of light.

1.4.2 Detector Response for GWs

The Interferometric gravitational wave detectors receive gravitational wave strain $h(t)$ as

$$h(t) = F_+ h_+(t) + F_\times h_\times(t) \tag{1.37}$$

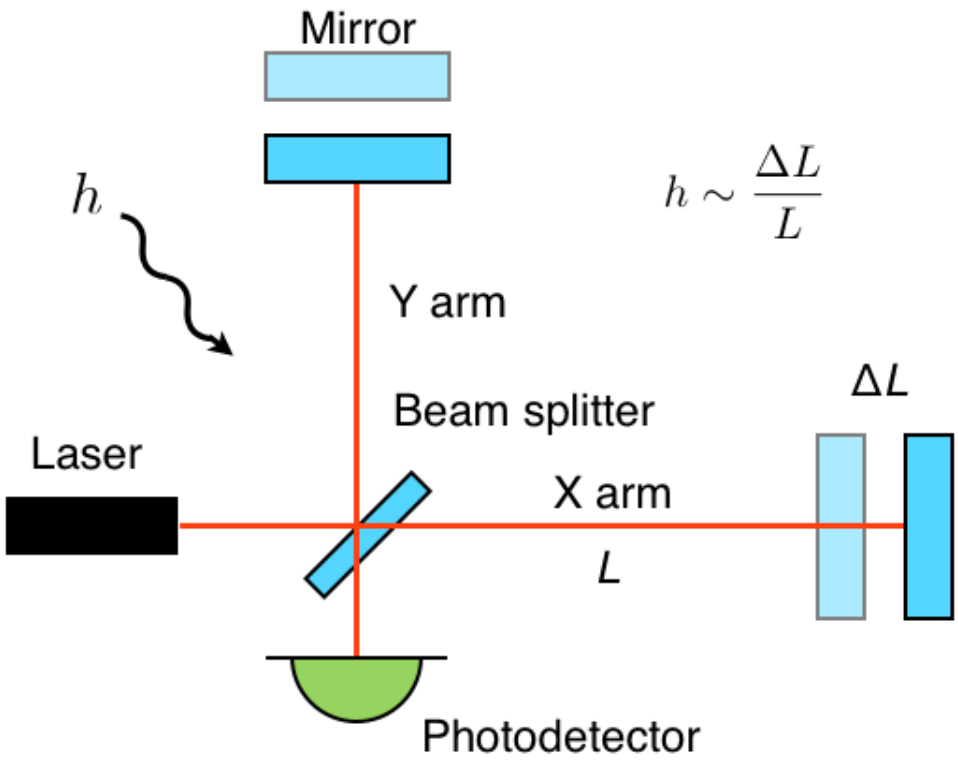

Figure 1.3: This is a simple Michelson interferometer. The simple Michelson consists of the laser, beam splitter, two mirrors, and photodetector. Gravitational waves are detected as a change of the intensity of the interference of light because the incident gravitational waves change the optical path length of two arms.

where the F_+ and $F_\times$ are the detector responses which are described as

$$F_+ = \frac{1}{2}(1+\cos^2\theta)\cos 2\phi\cos 2\psi + \cos\theta\sin 2\phi\sin 2\psi \quad (1.38)$$

$$F_\times = -\frac{1}{2}(1+\cos^2\theta)\cos 2\phi\sin\psi + \cos\theta\sin 2\phi\cos\psi \quad (1.39)$$

where θ is the angle between the z-axis and direction from the interferometer to the GW source, ϕ is the angle between the x-arm of interferometer and the projection of the direction from the interferometer to the GW source to detector plane, and ψ is the polarization angle. These angles and the response of detector are shown in FIG. 1.4.

At present the two advanced Laser Interferometer Gravitational wave Observatory (aLIGO) in Hanford, Washington and Livingston, Luisiana, the advanced Virgo(AdVirgo) in Pisa, Italy and the KAGRA in Kamioka, Japan are operating as kilo-metre scale interferometric detector. These detectors are expected to observe gravitational waves in simultaneously and to make up for the direction where the detector response is small each other.

1.4.3 Operating detectors

Four interferometric detectors which have kilo-metre scale of arms will be operated in the near future. The design sensitivities of these detectors are $h \sim 10^{-24}$ around a few hundred Hertz.

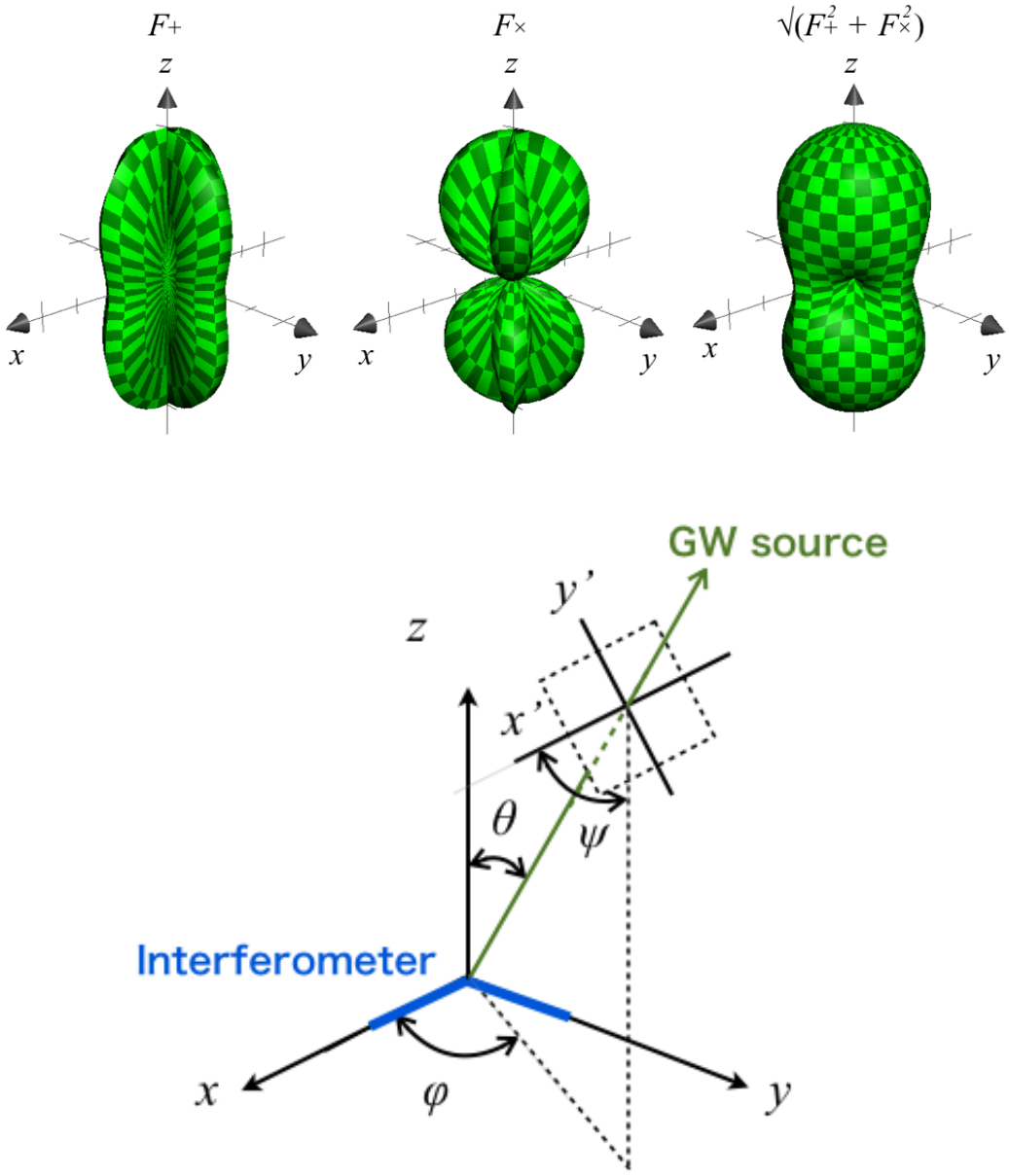

Figure 1.4: Top panel shows the detector response F_+^2 and $F_\times^2$ as the function of the sky location, θ, ϕ, and ψ.The definition of θ, ϕ, and ψ are shown in the bottom panel.

KAGRA

The Japanese gravitational wave detector which has 3km-arms, KAGRA[17], is constructed in the Kamioka mine. The uniqueness of KAGRA is the underground site and the use of cryogenic mirrors. These characteristics can contribute to reduce the seismic activity and the thermal noise. The design sensitivity of KAGRA is shown in FIG. 1.5

Advanced LIGO

The advanced LIGO is made up of two interferometric detectors which have 4km-arms. One of them is located in Hanford, Washington and another is located in Livingston, Luisiana. These two detectors are approximately aligned for the simultaneous observation. The design sensitivity is shown in FIG. 1.6

Advanced Virgo

The advanced Virgo(AdVirgo) is located in Pisa, Italy. AdVirgo has the 3km arms. The design sensitivity of AdVirgo is shown in FIG. 1.7.

1.4.4 Detector noise

The optical path length of the arms of the interferometer are changed by gravitational waves. They are also changed by the various noises. The principle noises of the gravitational wave detectors are the following.

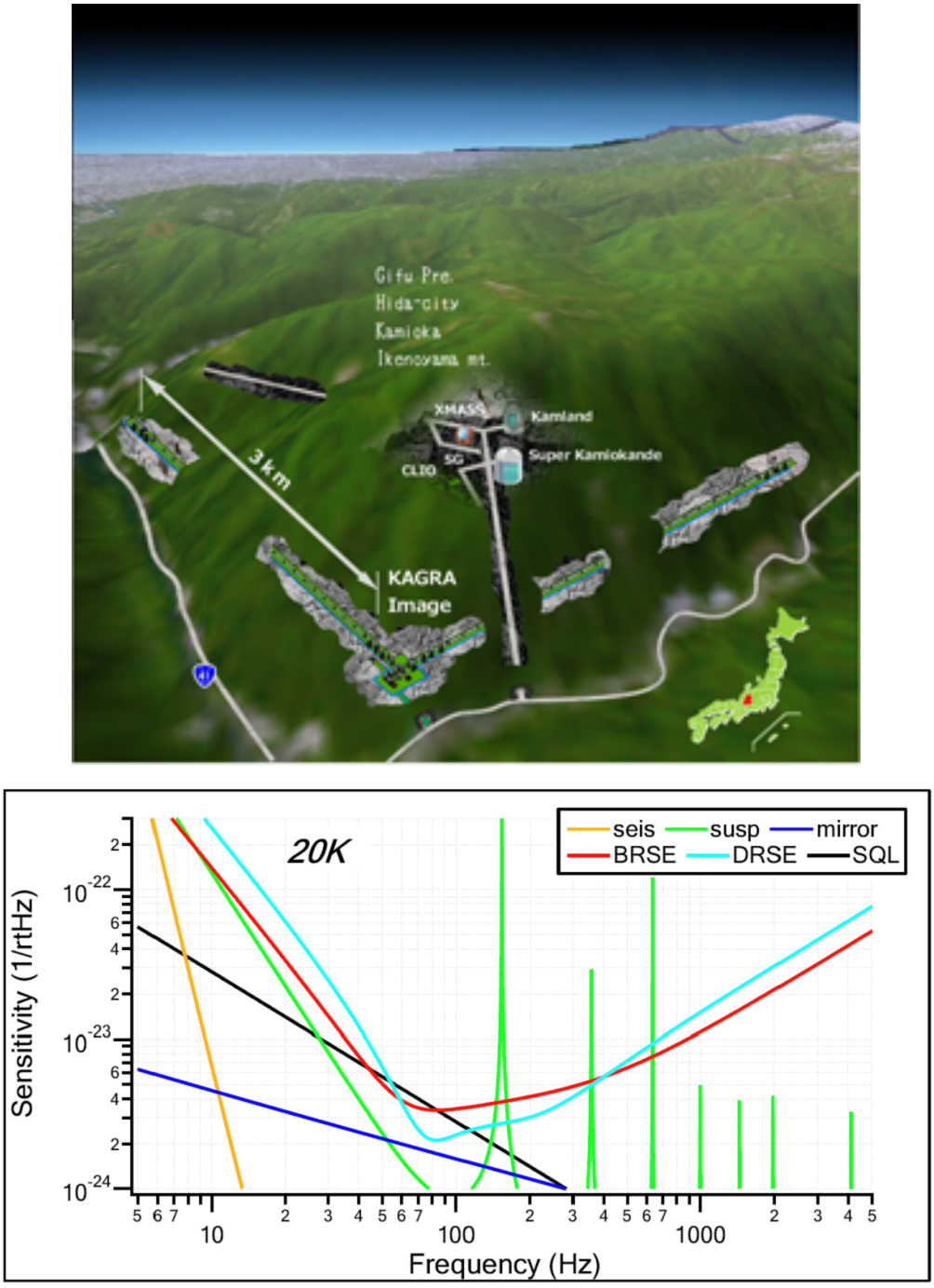

Figure 1.5: Top panel shows the image of a bird's-eye view of KAGRA[26]. Bottom panel shows the design sensitivity of KAGRA[27]. The vertical axis and horizontal axis represent the frequency and the strain equivalent value of the noise power spectrum density, respectively.

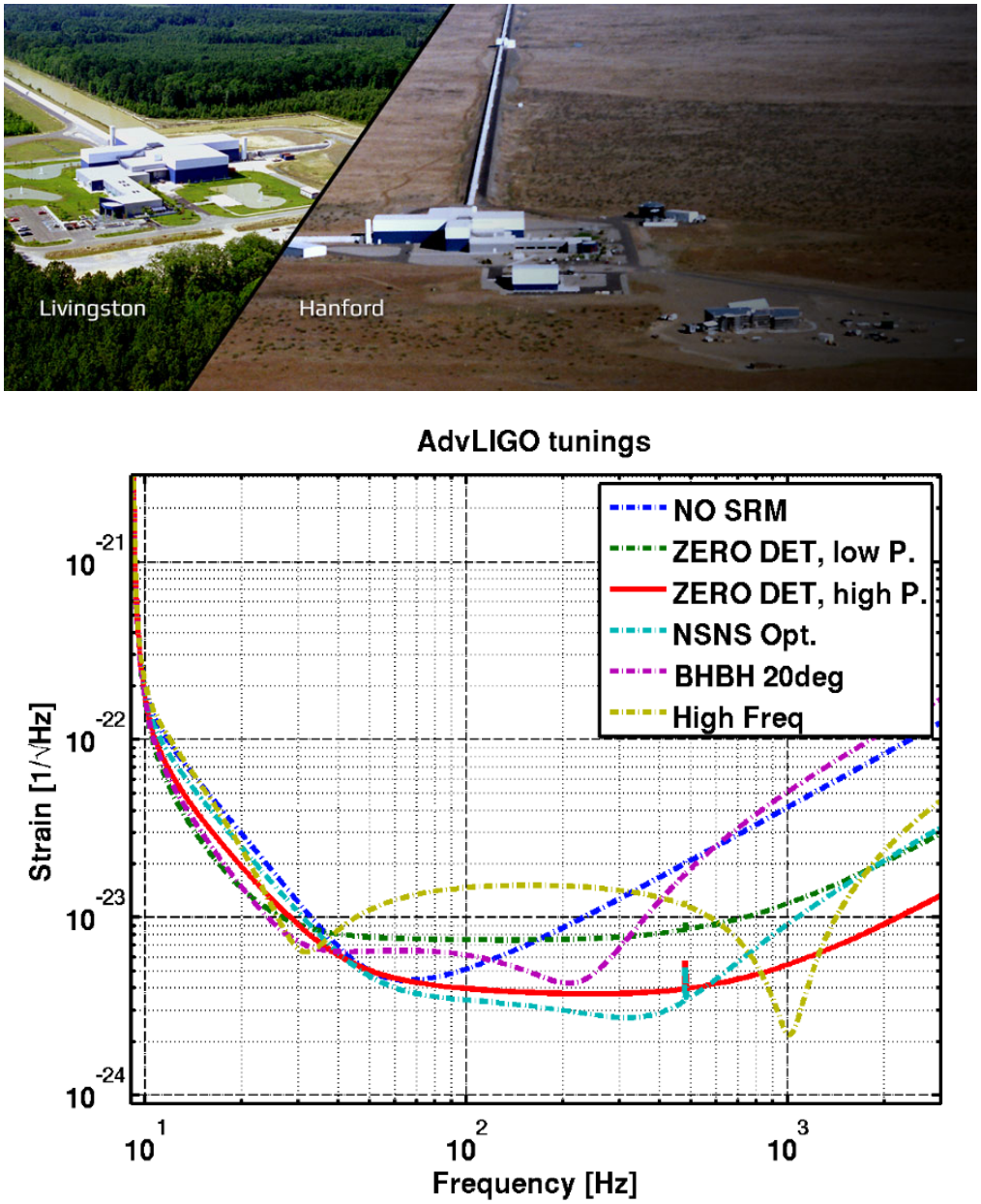

Figure 1.6: Top panel shows aerial photographs of advanced LIGO at Hanford and Livingston[28]. Bottom panel shows the design sensitivity of advanced LIGO[29]. The vertical axis and horizontal axis represent the frequency and the strain equivalent value of the noise power spectrum density, respectively.

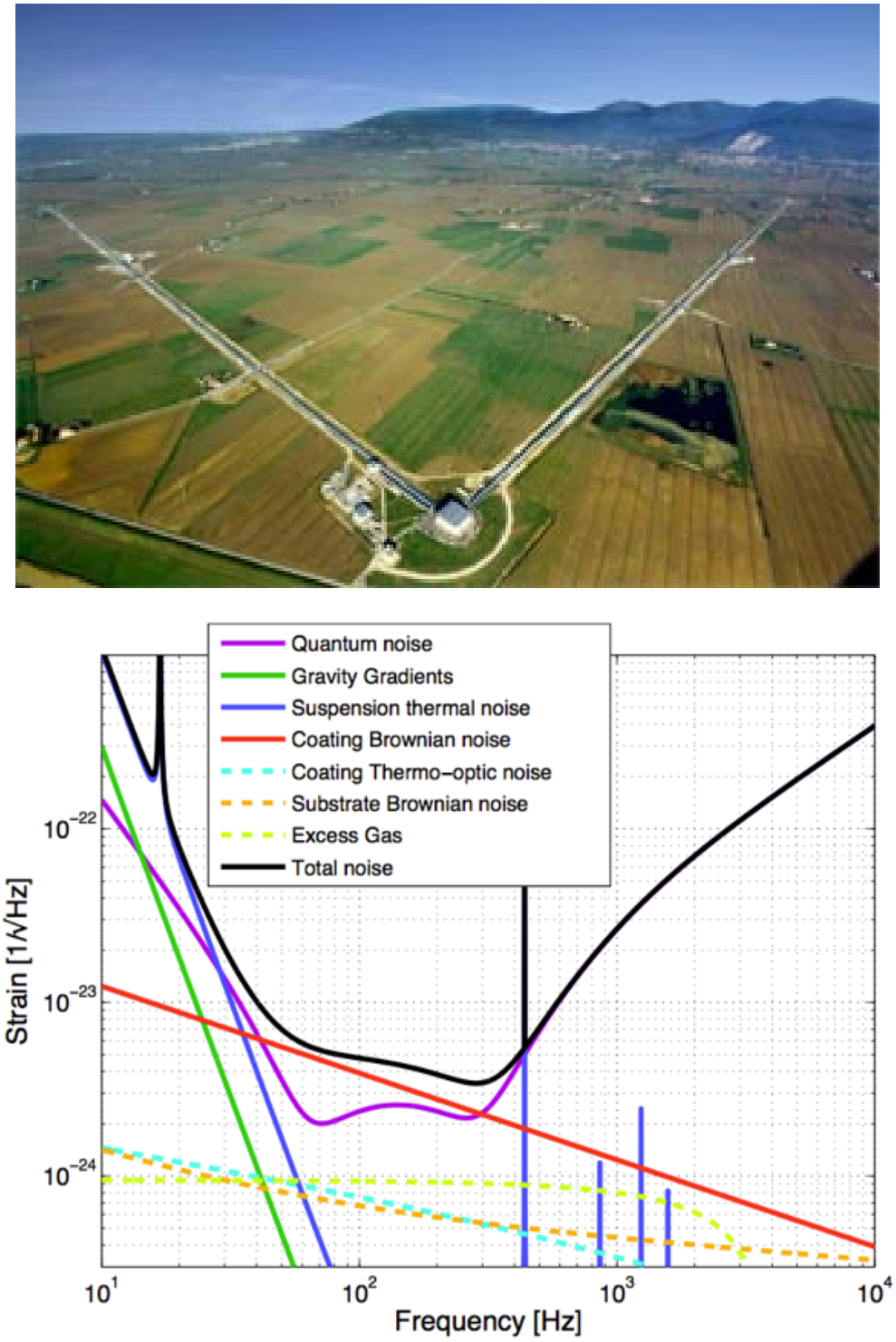

Figure 1.7: Top panel shows an aerial photograph of advanced Virgo[30]. Bottom panel shows the design sensitivity of advanced Virgo[31]. The vertical axis and horizontal axis represent the frequency and the strain equivalent value of the noise power spectrum density, respectively.

Seismic noise

The seismic activity shake the mirrors and change the optical path length. The power spectrum of the seismic activity follows

$$x_{\rm seis}(f) = 10^{-9} \times f^2 [\rm m/rHz] \tag{1.40}$$

where f is the frequency and 10^{-9} is a factor at the Kamioka mine[32]. The factor of power spectrum depends on the location of the detector. The noise caused by seismic activity is suppressed by the suspension system. Because the multistage pendulum is adopted as the suspension system, The drastic suppression of the seismic noise is realized in especially high frequency. Thus the seismic noise dominates only below about 10Hz in KAGRA, aLIGO, and AdVirgo

Shot noise and radiation pressure noise

The laser light passes through the arms of the interferometer. The shot noise is caused by the fluctuation of the photon number in statistically. The power spectrum of the shot noise follows

$$x_{\rm shot}(f) \propto \sqrt{\frac{\hbar c \lambda}{P}}, \tag{1.41}$$

where $\hbar$ is reduced Plank constant, c is the speed of light, λ is the wavelength of the laser light, and P is the laser power[33]. The shot noise is suppressed by increasing laser power. The mirrors are subjected to the radiation pressure when the laser light is reflected by mirrors. Then the position of the mirrors

fluctuates by fluctuation of the radiation pressure. The power spectrum of the radiation pressure noise follows

$$x_{\rm rad}(f) \propto \frac{1}{Mf^2}\sqrt{\frac{\hbar P}{c\lambda}}, \tag{1.42}$$

where M is a mass of the mirror[33]. The radiation pressure noise is suppressed by increasing the mass of mirrors or decreasing laser power.

We cannot reduce both radiation pressure noise and shot noise in the same time by changing for the laser power. We should set the laser power considering other noise sources and the frequency of gravitational waves.

Thermal noise

The suspension system and mirrors of the interferometer are excited by the Brownian motion because the temperature of the interferomter is finite. When we assume that the mechanical loss is absence, the power spectrum of the Brownian motion is given as

$$\langle x(\omega)\rangle^2 \sim \frac{4k_{\rm B}T}{M\omega_0^3 Q} \quad (\omega \ll \omega_0) \tag{1.43}$$

$$\sim \frac{4\omega_0 k_{\rm B}T}{M\omega^4 Q} \quad (\omega \gg \omega_0), \tag{1.44}$$

where $k_{\rm B}$ is the Boltzmann constant, T is a temperature, ω_0 is the resonance frequency, and Q is a quality factor[34]. The mirrors of interferometer is suspended to be behaved as free masses. The thermal fluctuation of the suspension system causes the vibration of the center of gravity of the mirrors. In general the resonance frequency of suspension system is around 1 Hz, so the power

spectrum of the thermal noise of suspension system in the frequency band in which we search for gravitational waves is given as

$$x_{\rm sus}(f) \propto \sqrt{\frac{T}{QM}} f^{-2}. \tag{1.45}$$

Elastic vibration of the mirrors is also excited by the thermal fluctuation. The shape of mirrors should be decided so that the resonance frequency of mirror is high enough compared to the frequency band in which we search for gravitational waves. Then the power spectrum of the thermal noise of mirror is given as[35]

$$x_{\rm mirror}(f) \propto \sqrt{\frac{T}{QM}}. \tag{1.46}$$

These thermal noise can be reduced by lowering the temperature of the suspension system and mirrors.

Chapter 2

Gravitational Wave Detector Noise Models

2.1 Detector noise and linear response system

In the search for gravitational wave, as described in Section 1.3, the behavior of the detection statistics can be described simply when the detector noise is Gaussian.

The gravitational wave detectors is the response system to grasp a small displacement. Such system can be regarded as linear response system locally. In the linear response system, a vibration mode of mechanical vibration can be regarded as a harmonic oscillator which follows,

$$m\ddot{\boldsymbol{x}} + \gamma\dot{\boldsymbol{x}} + k\boldsymbol{x} = 0. \tag{2.1}$$

Considering the case that this oscillator is subjected to a shaking force, the

motion of the oscillator can be described as

$$m\ddot{\boldsymbol{x}} + \dot{\boldsymbol{x}} + k\boldsymbol{x} = \boldsymbol{f}(t), \tag{2.2}$$

where $\boldsymbol{f}(t)$ is the shaking force and dot represents the derivative with respect to time.

The shaking force $\boldsymbol{f}(t)$ can be regarded as the sum of the infinitesimal pulsed forces. The total force subjected from t to $t + \Delta t$ can be described as

$$\boldsymbol{f}(t) = \frac{1}{\Delta t} \sum_j \boldsymbol{f}_j, \tag{2.3}$$

where $\boldsymbol{f}_j$ is the infinitesimal pulsed forces.

The total force, $\boldsymbol{f}(t)$ follows the Gaussian distribution by the central limit theorem when the following conditions are satisfied; (1) The shaking force is random.;(2) The shaking force is continuous. In other words, a number of the summation in Eq. (2.3) is large enough. (3) The standard deviation of $\boldsymbol{f}(t)$ is finite and is not zero.

The mechanical vibration is Gaussian when the shaking force is Gaussian on the linear response system. In Gravitational wave detectors, detector noise can be regarded as Gaussian noise as far as above three conditions are satisfied. On the other hand, when these conditions are not satisfied due to, for example, the presence of the discrete force, the detector noise does not follows Gaussian distribution. In addition to this, the detector noise does not follows Gaussian distribution when the gravitational wave detectors cannot be regarded as linear response system even though the shaking force is Gaussian.

2.2 Gaussian Noise

The noise of gravitational wave detector contains various sources. Principle noise components are seismic activity, thermal noise, radiation pressure noise and photon shot noise. These noise were assumed to be Gaussian in many earlier theoretical studies[36] because the deviations from Gaussian distribution can often be regarded as the non-stationary noise and the statistical treatment of the Gaussian behavior is easier than that of the non-Gaussian behavior.

In the case of Gaussian noise, the real part $\Re[\tilde{n}(f)]$ and imaginary part $\Im[\tilde{n}(f)]$ of the Fourier transform of detector noise $\tilde{n}(f)$ follow the Gaussian distribution,

$$p_{\mathrm{G}}(x) = \frac{1}{\sqrt{2\pi}\sigma} \exp\left(-\frac{x^2}{2\sigma^2}\right), \tag{2.4}$$

where x is either $\Re[\tilde{n}(f)]$ or $\Im[\tilde{n}(f)]$ and σ is the standard deviation of x. The absolute value of $\tilde{n}(f)$, $|\tilde{n}(f)|$, then follows Rayleigh distribution,

$$p_{\mathrm{R}}(x) = \frac{x}{\sigma^2} \exp\left(-\frac{x^2}{2\sigma^2}\right), \tag{2.5}$$

where x is $|\tilde{n}(f)|$.

Unfortunately, it is known from the experiences of the GW searches[37, 38] that the detector noise includes non-stationary and/or non-Gaussian noise components. Some examples of the histogram of the $|\tilde{n}(f)|$ of LIGO S5 observational data are shown in FIG. 2.1. The amplitude spectrum $|\tilde{n}(f)|$ is calculated per 1 second and these histograms contains the 1024 second long data. The behavior of the tail of the distribution of the detector noise are

difference between the top panel and bottom left panel in FIG. 2.1. The bottom right panel in FIG. 2.1 shows the noise distribution which contains some outliers. Because misreading the noise distribution increase the false events caused by the detector noise, evaluating the noise distribution is important for reliable detection of gravitational waves. Evaluating mean or variance of noise is one of the useful method for understanding noise behavior. However when the detector noise contains outliers originated from non-stationary noise, it is difficult to estimate mean and variance of the stationary noise. In this kind of situation, it is useful to use cumulative distribution or quantiles of the noise for characterizing the behavior of the stationary noise since cumulative distribution and quantiles are more robust for outliers than high-order moments. Because these non-Gaussian distributed noise tend to have a heavy tail, estimating a quantile of noise distribution is one of the effective measure.

2.3 Realistic Detector Noise

The assumption that the detector noise follows Gaussian distribution often good as zeroth order approximation. However we can not always adopt this approximation because there are cases when non-Gaussianity and non-stationarity dominate in a certain time or frequency band. The non-Gaussianity and the non-stationarity make the false alarm rate increase and make it hard to estimate behavior of noise such as noise power spectrum of stationary and stable

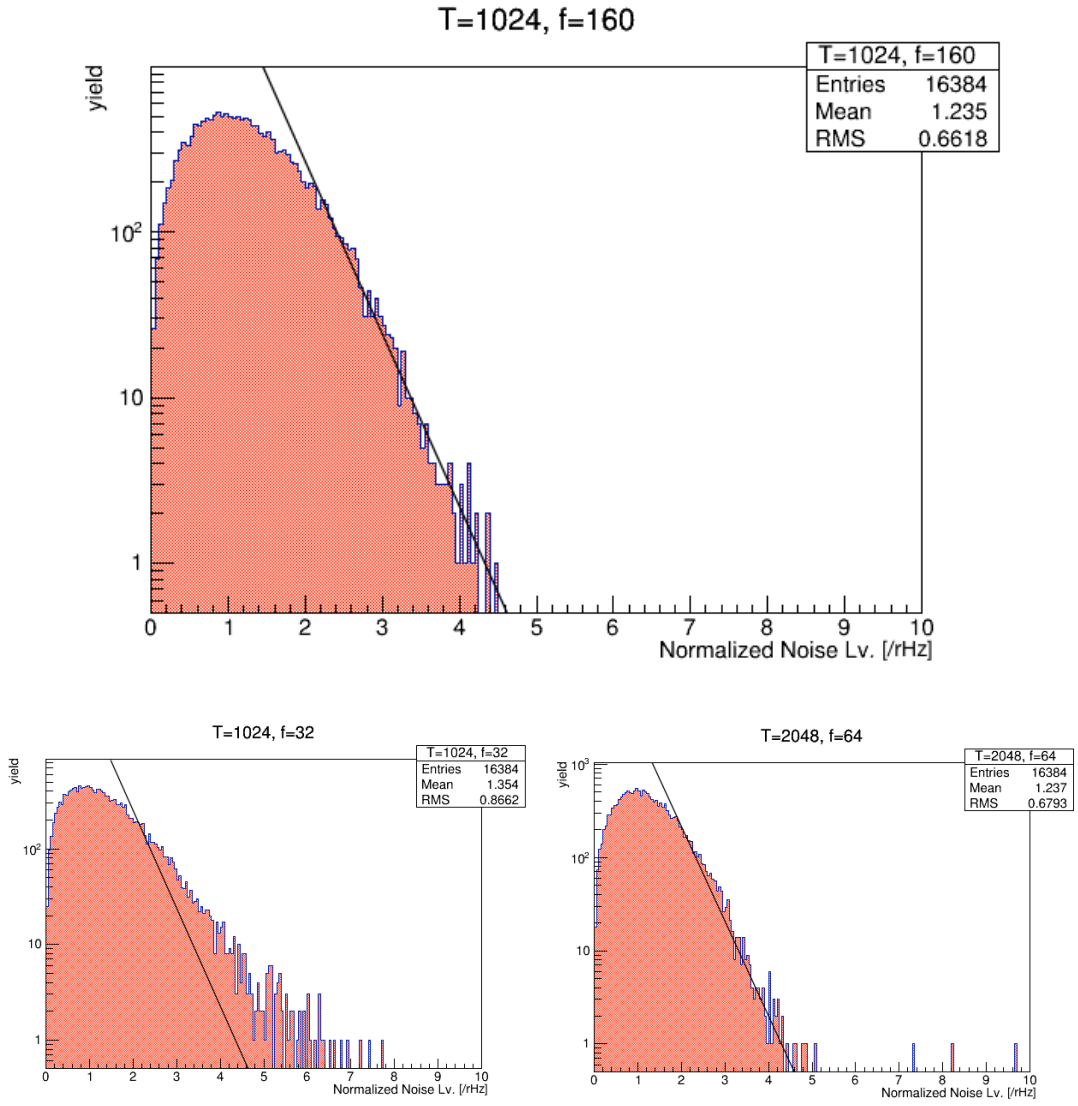

Figure 2.1: These plot show the histogram of the $|\tilde{n}(f)|$ of LIGO S5 Observational data. The amplitude spectrum $|\tilde{n}(f)|$ is calculated per 1 second and these histograms contains the 1024 second long data.

component of noise.

Fig. 2.2 shows the normalized noise level of LIGO data[39, 40] as a function of frequency. The data used was taken from the GPS time 842747904 to 842764288. This figure shows that the LIGO data is not an ideal Gaussian noise especially in low frequency band. According to the results of the LIGO observation, the false events caused by detector noise were greater than the ones which is estimated in the case that the detector noise follows Gaussian distribution[8, 41]. Non-Gaussianity in low frequency shown in FIG. 2.2 is probably one of the cause of increasing false events. Although the non-Gaussian noise are not always dominant, we find the non-Gaussianity in a certain time and frequency region such as Fig. 2.2.

The matched filtering method which is most popular method to search for gravitational waves from compact binary coalescences is optimal in the case of Gaussian noise (see Chapter 4). There are many cases that the tail of detector noise distribution is larger than the Gaussian distribution. In these cases, the estimated power spectrum of the detector noise is contaminated by noise which belongs to outlier. Moreover the noise events with high signal-to-noise ratio increase because the higher order moment such as variance of heavy tail distribution is larger than the Gaussian distribution. When the detector noise contains non-Gaussian and non-stationary noise component, using the search method that assumes the Gaussian noise may become serious problem especially in the era of the detection of GWs, since the detection

with low signal-to-noise ratio is predicted especially in the initial phase of GW detection. Reducing false alarm is also important for using possession time of other detectors in the multi-messenger survey.

Through the past observation runs of LIGO and Virgo, there have been a lot of efforts to improve the performance of the GW searches by identifying and eliminating narrow-band and transient non-stationary noise events contained in the detector noise[38, 42, 43, 44, 45]. Identification of noise sources and their removal have been done by evaluating non-stationarity of the many auxiliary channels of the GW detector from the perspective of telescope diagnosis[46, 47].

Moreover some new methods that is robust against contamination by non-Gaussian noise was suggested[48, 49] and showed that the performance of a matched filtering method for a GW from a compact binary coalescence from the data of the fifth Science run (S5) of LIGO was improved compared with the method based on the Gaussian noise model[50, 51, 52]. In these works, non-Gaussian noise was not distinguished from non-stationary in explicitly. Although [50] focused on stationary non-Gaussian noise by using Student-t noise model and the parameter ν of Student-t distribution as an indicator of non-Gaussianity, the accuracy and precision of ν which is estimated from detector data were not discussed. We will explain the Student-t noise model in next section and will investigate the accuracy and precision of ν in order to reveal the domination of the non-Gaussianity statistically (see Chapter 3). Investigating such non-Gaussianity may improve the GW-search performance

compared with the method based on Gaussian noise model by ignoring such non-Gaussianity. So investigating non-Gaussianity enables us to use the detector signal with poor quality.

2.4 Non-Gaussian Noise Model

The non-Gaussian components in the GW detector noise make the false alarm rate increase and make it hard to estimate behavior of noise such as noise power spectrum. There is a possibility to suppress these false events by quantifying weight of tail of the noise distribution. We introduce the Student-t distribution for evaluating weight of tail of the distribution.

The Student-t noise model is known as one of the non-Gaussian noise models which is a natural extension of Gaussian noise model[53]. In this model $\Re[\tilde{n}(f)]$ and $\Im[\tilde{n}(f)]$ follow the Student-t distribution,

$$p_{\mathrm{ST}}(x) = \frac{\Gamma(\frac{\nu+1}{2})}{\sqrt{\nu\pi}\sigma_s\Gamma(\frac{\nu}{2})}\left(1+\frac{1}{\nu}\left(\frac{x}{\sigma_s}\right)^2\right)^{-\frac{\nu+1}{2}}, \tag{2.6}$$

where x is either $\Re[\tilde{n}(f)]$ or $\Im[\tilde{n}(f)]$, σ_s is a scaling parameter and ν is a positive value which characterizes the weight of the tail of the distribution. The scaling parameter can be described with standard deviation σ of $\tilde{n}(f)$ and ν as

$$\sigma_s = \sigma\sqrt{\frac{\nu-2}{\nu}}. \tag{2.7}$$

$|\tilde{n}(f)|$ then follows the Student-Rayleigh distribution,

$$p_{\mathrm{SR}}(x) = \frac{x}{\sigma_s^2}p_{F(2,\nu)}\left(\frac{x^2}{2\sigma_s^2}\right) \tag{2.8}$$

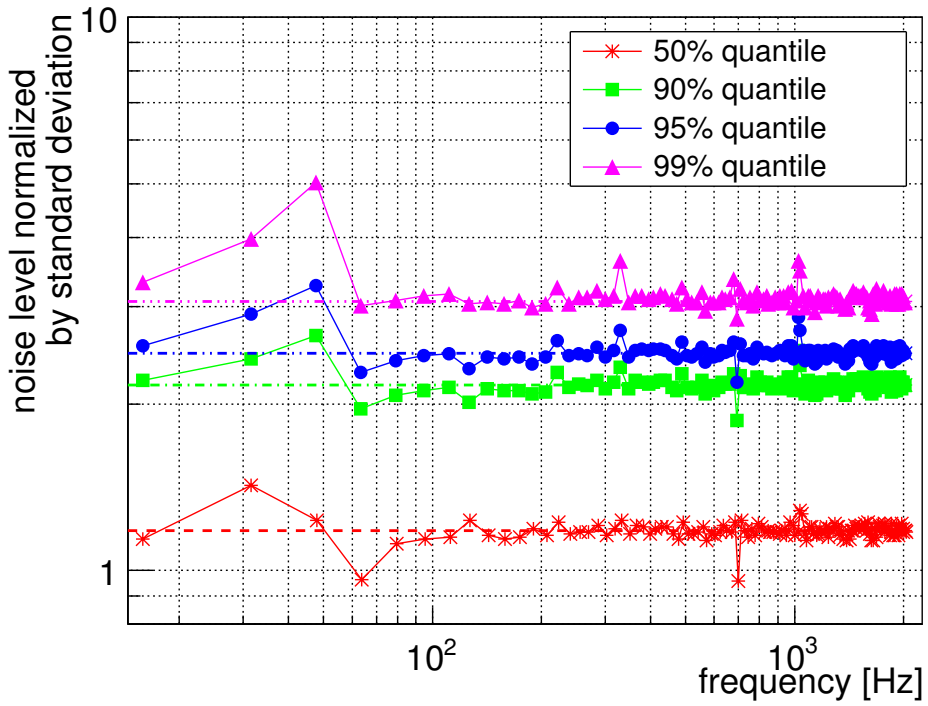

Figure 2.2: This plot shows the 50%(Red stars), 90%(Green filled square), 95%(Blue filled circles), and 99%(Pink filled triangle) quantiles of the distribution of the LIGO S5 data taken from GPS time 842747904 to 842764288. Each quantile was calculated from 2^{18} samples in every 16Hz. Dashed line, a dot chain line, a two-dot chain line and a three-dot chain line represent the 50%, 90%, 95% and 99% quantiles expected if the data follows Gaussian distribution respectively. This figure indicates detector noise deviates from Gaussian distribution especially in low frequency band.

where x is $|\tilde{n}(f)|$and $p_{F(2,\nu)}$ is the probability density function of the F-distribution with the degrees of freedom $(2, \nu)$[54, 55]. The relation between the scaling parameter, σ_s, and standard deviation of $\Re[\tilde{n}(f)]$ and $\Im[\tilde{n}(f)]$, σ, is Eq. (2.7).If the variance σ^2 of the detector noise is *a priori* known, some of the statistical properties of our estimator of ν can be calculated analytically. Unfortunately, σ^2 is unknown in general and we must estimate σ^2 from detector noises. So we investigate statistical properties of an estimator of ν by plugging the sample estimate of σ into the expressions. It is noted that Eq. (2.6) and Eq. (2.8) are Gaussian and Rayleigh distribution in $\nu \to \infty$ limit. The Rayleigh and Student-Rayleigh distributions with ν of 4, 8, 16 and 64 are shown in Fig. 2.3. The weight of the tail is characterized by the parameter ν[56].

It is useful to use ν as a measure which characterizes the deviation from Gaussianity, because the detector noise is known to follow a heavy tail distribution and this noise tail distribution increases false alarm events.

It is not necessary for using ν as the indicator of non-Gaussianity that the detector noise always follows the Student-t distribution. In this kind of situation, though we cannot determine the strict distribution of the detector noise using ν, ν can shows the weight of the tail of noise distribution.

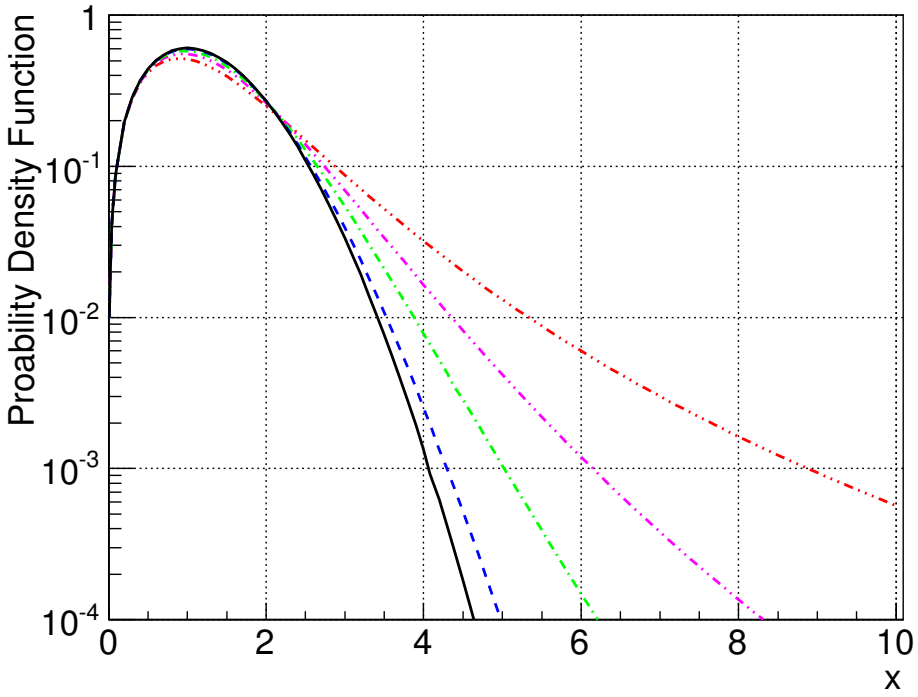

Figure 2.3: This plot shows Rayleigh distribution(Black solid line) and Student-Rayleigh distribution functions with $\sigma_s = 1$ for various ν. Each color means $\nu = 4$(Blue dashed line), $\nu = 8$(Green 1-dot chained line), $\nu = 16$(Pink 2-dot chained line) and $\nu = 64$(Red 3-dot chained line). In small ν case, the tail of distribution is large. On the other hand, the Student-Rayleigh distribution is closer to Rayleigh distribution for large ν.

Chapter 3

Characterization of Detector Noise

3.1 Data Processing of Estimating ν

We quantify the non-Gaussianity of detector noise by using Student-t noise model and parameter ν. An algorithm to estimate ν from the detector noise is shown in Fig. 3.1. Let us denote the total data length in seconds by T and the sampling frequency in Hz by f_s, and the product of the two by $2M$ (assuming M to be an integer for simplicity). Detector output discrete time series $n(t_k)$ $(k = 1, ..., 2M.)$ is divided into N chunks $n_i(t)$ with each $t_{\rm FFT} = T/N$ seconds. Then time series data of each chunk $n_i(t)$ is Fourier transformed into $\tilde{n}_i(f_j)$ $(j = 1, ..., M.)$. We then estimate the parameter ν for the i-th chunk at the coarse frequency bin α using l samples around the bin.

Specifically, the estimator ν, denoted by $\hat{\nu}_i(f_\alpha)$ is calculated from l samples of $\tilde{n}_i(f_j)$ $(j = \alpha - l/2, ..., \alpha + l/2)$ using the method explained below. The frequency resolution of $\hat{\nu}_i(f_\alpha)$ is determined by l such that $\delta F = l/t_{\rm FFT} > 1/T$.

The p-quantile, Q_P, is sought from l-sample data around α-th bin in frequency domain. The estimator $\hat{\nu}$ is defined as

$$\hat{\nu} \equiv \arg\min_{\nu} |Q_P - Q_{SR}(\sigma_s, \nu;\ P)| \tag{3.1}$$

where $Q_{\rm SR}(\sigma_s, P;\ \nu)$ is the theoretical quantile function of Student-Rayleigh distribution.

The cumulative distribution function and quantile function of Student-Rayleigh distribution are described as

$$P_{\rm SR}(\nu, \sigma_s;\ x) = 1 - \left(1 - \frac{(x/\sigma_s)^2}{\nu + (x/\sigma_s)^2}\right)^{\nu/2} \tag{3.2}$$

and

$$Q_{\rm SR}(\nu, \sigma_s;\ P) = \sigma_s \sqrt{\frac{\nu(1 - (1-P)^{2/\nu})}{(1-P)^{2/\nu}}} \tag{3.3}$$

respectively.

Although we do not know the true value of σ_s of $\tilde{n_i}(f_j)$ in general, standard deviation σ of $\tilde{n_i}(f_j)$ is estimated as

$$S_n(f) = \frac{< \tilde{n}(f)\ \tilde{n}^*(f) >}{t_{\rm FFT}} \tag{3.4}$$

$$= \frac{2\sigma^2}{t_{\rm FFT}}. \tag{3.5}$$

In other words, σ_s can be estimated as

$$\sigma_s = \sigma\sqrt{\frac{\nu - 2}{\nu}} = \sqrt{\frac{\nu - 2}{\nu} S_n(f) t_{\rm FFT}}. \tag{3.6}$$

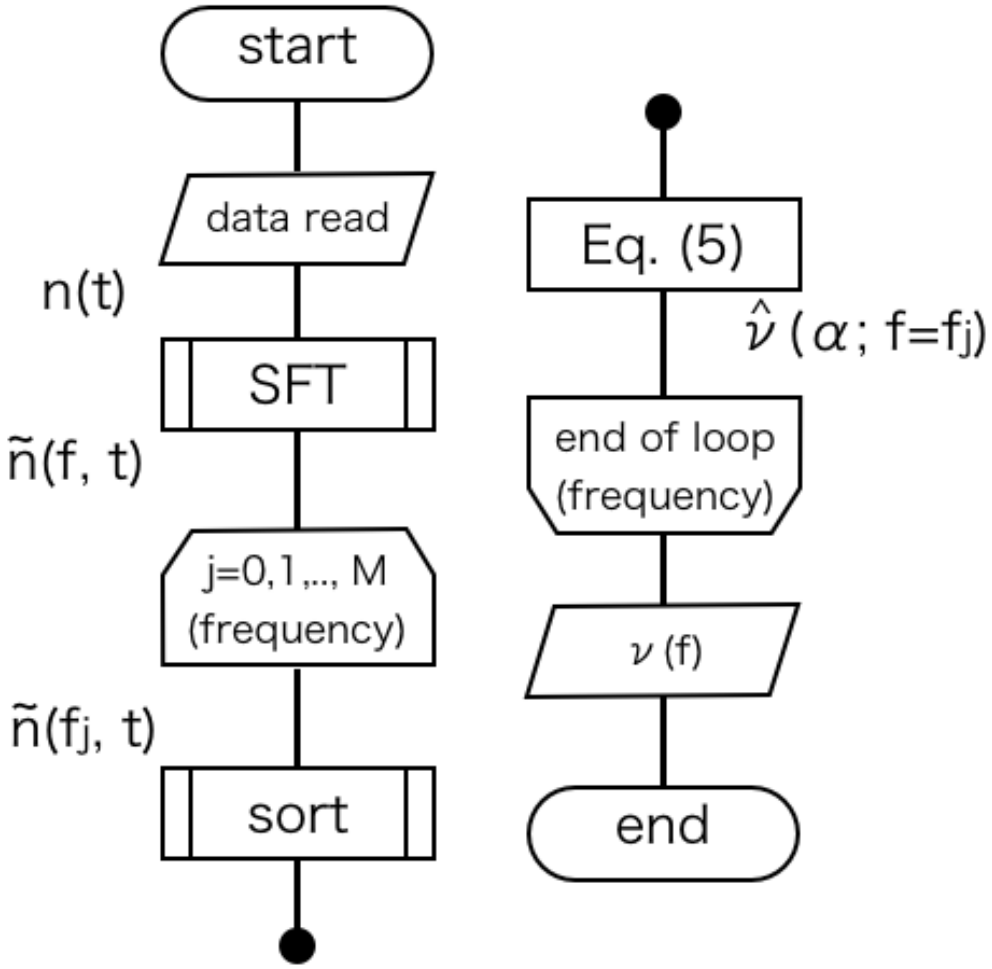

Figure 3.1: The algorithm of estimating $\hat{\nu}$ from the detector noise.

So using normalized noise, $|\tilde{n_i}(f_j)|/\sqrt{S_n(f)t_{\rm FFT}}$ instead of $|\tilde{n_i}(f_j)|$, by the standard deviation instead of $|\tilde{n_i}(f_j)|$ allows that we use the description eliminating σ_s,

$$Q'_{\rm SR}(\nu;\ P) = \sqrt{\frac{(\nu-2)(1-(1-P)^{2/\nu})}{(1-P)^{2/\nu}}} \tag{3.7}$$

as the quantile function of Student-Rayleigh distribution instead of Eq. 3.3.

3.2 Rejection test of Gaussian noise hypothesis

This section shows the response of estimator $\hat{\nu}$ for Gaussian noise. Strictly speaking, $\hat{\nu}$ estimated from Gaussian noise is infinity. However we obtained $\hat{\nu}$ as finite value because $\hat{\nu}$ is estimated from finite samples. We introduce the threshold on $\hat{\nu}$ above which data follows Gaussian distribution taking account of dependency on data length. Fig. 3.2 shows the histograms of obtained $\hat{\nu}$. Data sets of detector noise are generated by pseudo random numbers which follow Guassian distribution. We test the method for estimating $\hat{\nu}$ using the data whose lengths T are 128, 256, 512, 1024, 2048 and 4096s. The p-value and entry numbers of all histograms are 0.99 and $524,288$.

The thick red region represents 1% lower tail of the $\hat{\nu}$ distribution. If we take 1% ($\alpha = 0.01$) significant level, the corresponding region is $\hat{\nu} < \nu_{\alpha=0.01,T=4096s} = 91.4$. Hence, we can reject the null-hypothesis that data follows Gaussian distribution by 99% confidence if we set the threshold $\nu_{\alpha=0.01,T=4096s} = 91.4$, modulo the error inherited in our Monte Carlo simulations.

The ν_α depends on the data length T. FIG. 3.3 shows the ν_α with $T = 128, 256, 512, 1024, 2048$, and 4096s.

Long data length is favorable for detecting non-Gaussianity in the detector noise. However it is difficult to choose the long data length like as a day, a week, etc. because our method assumes the stationarity of data during the

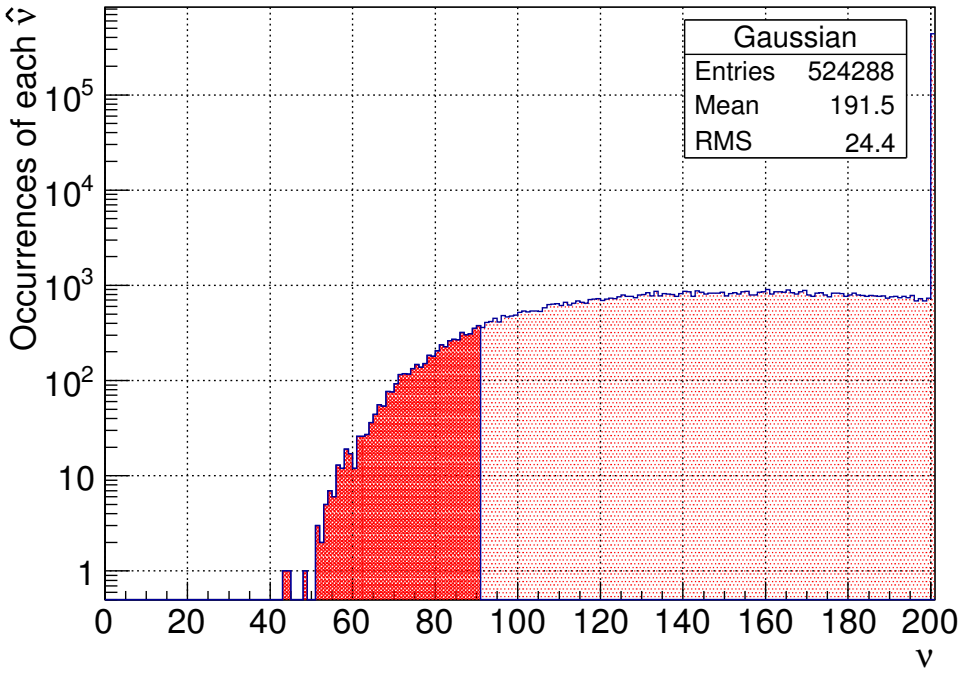

Figure 3.2: The resulting histogram of the estimated $\hat{\nu}$'s for 524,288 sets of simulated Gaussian noise data. The data length of the simulated noise is 4096s. This figure shows that even for purely Gaussian noise, $\hat{\nu}$ can be small with a non-negligible probability. The critical region for rejecting Gaussianity is determined by the histogram. When data length $T = 4096$s, $\nu_{th} = 91.4$.

data length T.

In LIGO experience, the stationarity of detector noise can be regarded during a few hours in typically[41]. A excess power method for searching gravitational wave burst typically regarded the detector noise as stationary during a few minutes[57].

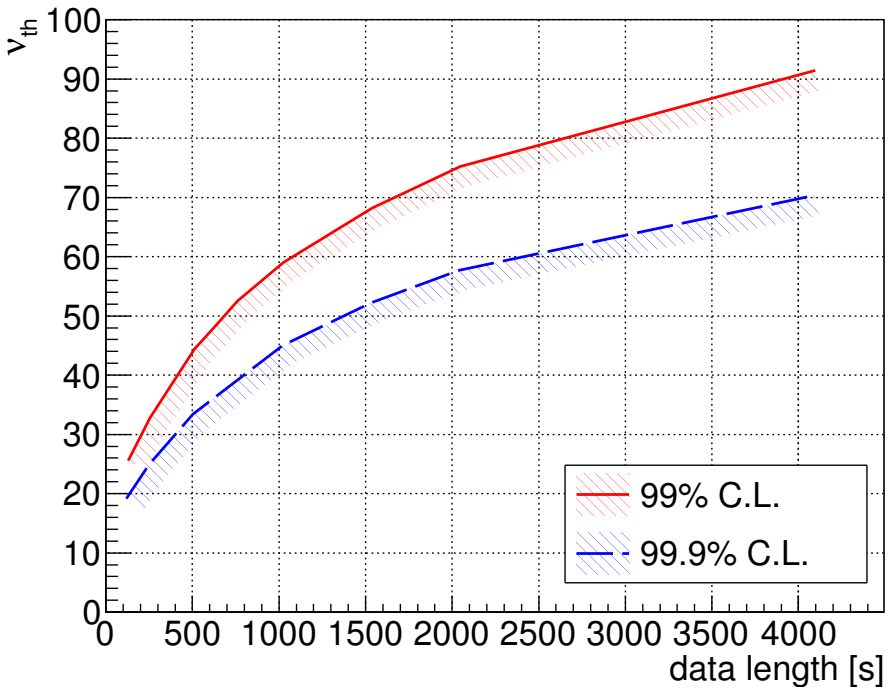

Figure 3.3: This plot shows the critical regions for rejecting Gaussianity with significance levels of 1% and 0.1%. In the lower region of each line, Gaussian noise hypothesis is rejected with 99%(red) and 99.9%(blue) confidence. e.g. when ν is estimated from 1024 second long data, the hypothesis of Gaussianity is rejected if $\nu \leq 59.0$ with 99% confidence.

3.3 The precision of the ν as the indicator of non-Gaussianity

In this section, we discuss the precision of $\hat{\nu}$. The tail of distribution of Student-Rayleigh model rapidly gets heavy in small ν. On the other hand when ν is large, the non-Gaussianity is not significant, and the tail of distribution gently gets heavy. So precision of $\hat{\nu}$ depends on ν.

In order to evaluate the degree of non-Gaussianity quantitatively it is important to investigate the confidence interval of ν. Now, we prove that our estimator of ν is strongly consistent, therefore asymptotically unbiased.

proposition. $\hat{\nu}$ is strongly consistent.

proof. We define $Q_{\mathrm{SR}\{n\}}(p,\nu)$ as a p-quantiles of n samples distributed in Student-Rayleigh function. By the strong law of large number at a given ν,

$$Q^{-1}_{\mathrm{SR}\{n\}}(Q_{\mathrm{SR}}(p,\nu)) \to Q^{-1}_{\mathrm{SR}}(Q_{\mathrm{SR}}(p,\nu)), \quad \text{almost surely.} \tag{3.8}$$

Since $p = Q^{-1}_{\mathrm{SR}\{\mathrm{n}\}}(Q_{\mathrm{SR}\{n\}}(p,\nu)) = Q^{-1}_{\mathrm{SR}}(Q_{\mathrm{SR}}(p,\nu))$,

$$Q_{\mathrm{SR}\{n\}}(p,\nu) \to Q_{\mathrm{SR}}(p,\nu), \quad \text{almost surely,} \tag{3.9}$$

by the continuous mapping theorem. $\hat{\nu} \to \nu$ is proved by applying continuous mapping theorem again because Eq. (3.3) is also the continuous function of ν.

□

Confidence interval of ν is difficult to calculate because $\hat{\nu}$ is not asymptotic normal and in general, we do not know the true variance of detector noise. However, confidence interval can be approximated in the following sense[58].

By simulations using Student-t noise model with various ν, we can find $\nu_{\rm lower}(\nu)$ and $\nu_{\rm upper}(\nu)$ such that $P(\nu_{\rm lower} < \hat{\nu} < \nu_{\rm upper}) = 1 - \alpha$. On the other hand a confidence interval is $[\hat{\nu}_{\rm lower}, \hat{\nu}_{\rm upper}]$, such that $P(\hat{\nu}_{\rm lower} < \nu < \hat{\nu}_{\rm upper}) = 1 - \alpha$. Here we propose $\hat{\nu}_{\rm lower} := \nu_{\rm lower}(\hat{\nu})$ and $\hat{\nu}_{\rm upper} := \nu_{\rm upper}(\hat{\nu})$. Although there is no rigorous reason why $P(\hat{\nu}_{\rm lower} < \nu < \hat{\nu}_{\rm upper}) = P(\nu_{\rm lower}(\hat{\nu}) < \nu < \nu_{\rm upper}(\hat{\nu}))$ equals $1-\alpha$, we use $[\nu_{\rm lower}(\hat{\nu}), \nu_{\rm upper}(\hat{\nu})]$ instead of confidence interval.

$\nu_{\rm upper}$ and $\nu_{\rm lower}$ can be calculated as follows. Fig. 3.4 shows the histograms of $\hat{\nu}$ estimated from the Student-t noise with $\nu = 25$.

The configuration of this simulation is the same as in previous Gaussian simulation (524,288 sets of simulation noise and data length $T = 4096$s). The ν of the simulated Student-t noise is 25. The thick red region represents 1% upper $\nu_{\rm upper}$ and lower $\nu_{\rm lower}$ tails of $\hat{\nu}$. The corresponding ν are $23.4, 48.8$, respectively. We performed the same simulations using simulated Student-t noise changing ν from 8 to 50. Fig. 3.5 shows $\nu_{\rm lower}$ and $\nu_{\rm upper}$ as the function of $\hat{\nu}$. In Fig. 3.5, the red solid line and the blue dashed line represent the lower ($\nu_{\rm lower}$) and the upper ($\nu_{\rm upper}$) boundaries of the 98% and 99.8% confidence region respectively. Confidence interval is in between $\nu_{\rm lower}$ and $\nu_{\rm upper}$. When $\hat{\nu} = 25$, 98% confidence interval is $15.45 \leq \nu \leq 27.29$. The confidence interval becomes wider rapidly as ν become larger.This behaviour of confidence interval

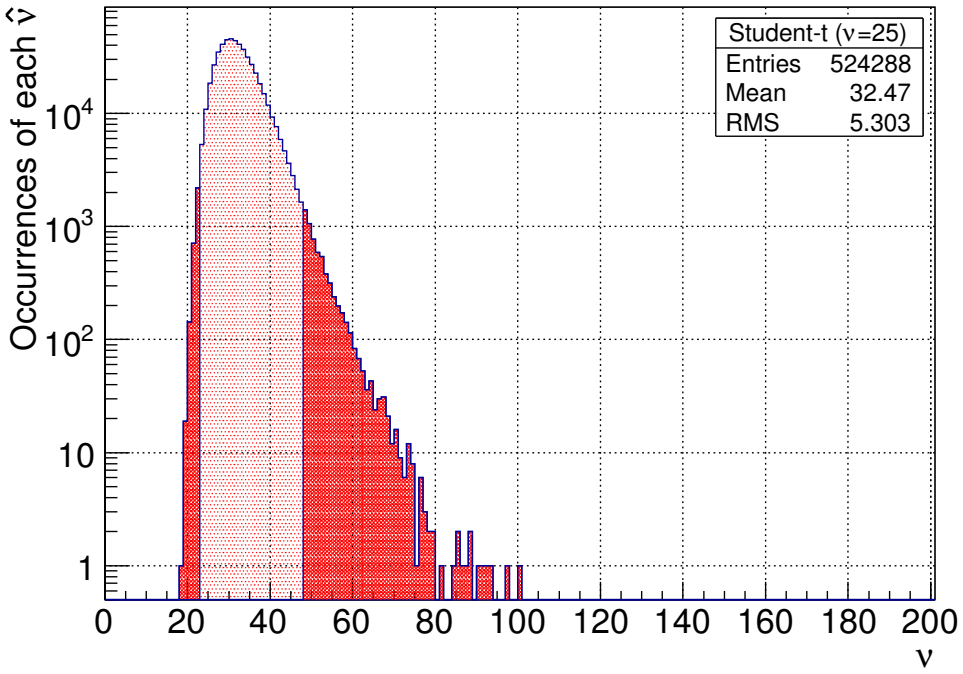

Figure 3.4: This plot shows result of estimated ν for 524,288 sets of simulated Student-t noise in case of $\nu = 25$. Estimated ν fluctuate and 1% confidence upper(ν_{upper}) and lower(ν_{lower}) boundary are $\nu_{\text{upper}} = 48.8$ and $\nu_{\text{lower}} = 23.4$.

comes from the fact that the shape of the Student-Rayleigh distribution is more sensitive to the change of ν in the case of small ν than the in case of large ν.

Fig. 3.6 shows the dependence of the confidence interval on the data length T. The upper and the lower red line represent ν_{upper} and ν_{lower} in the case of Student-t noise with ν of 25 as a function of T. The confidence interval of $\hat{\nu}$ gets monotonically narrower. When $T = 2048, 4096$, the 98% confidence intervals are $14.52 \leq \nu \leq 29.91$, $15.45 \leq \nu \leq 27.29$, respectively.

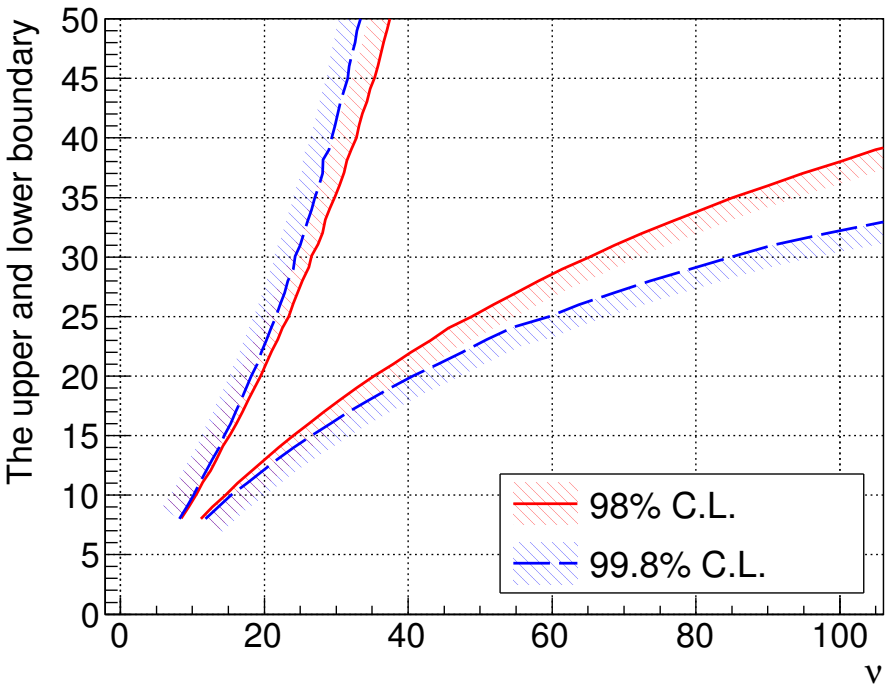

Figure 3.5: This plot shows the 98%(Red line) and 99.8%(Blue line) confidence interval of ν when estimation time is 4096s. For small ν value, resolution of ν is good. For example, when we obtain $\nu = 25$ in case of 4096s estimation time, 98% confidence interval of ν is $15.45 \leq \nu \leq 27.29$

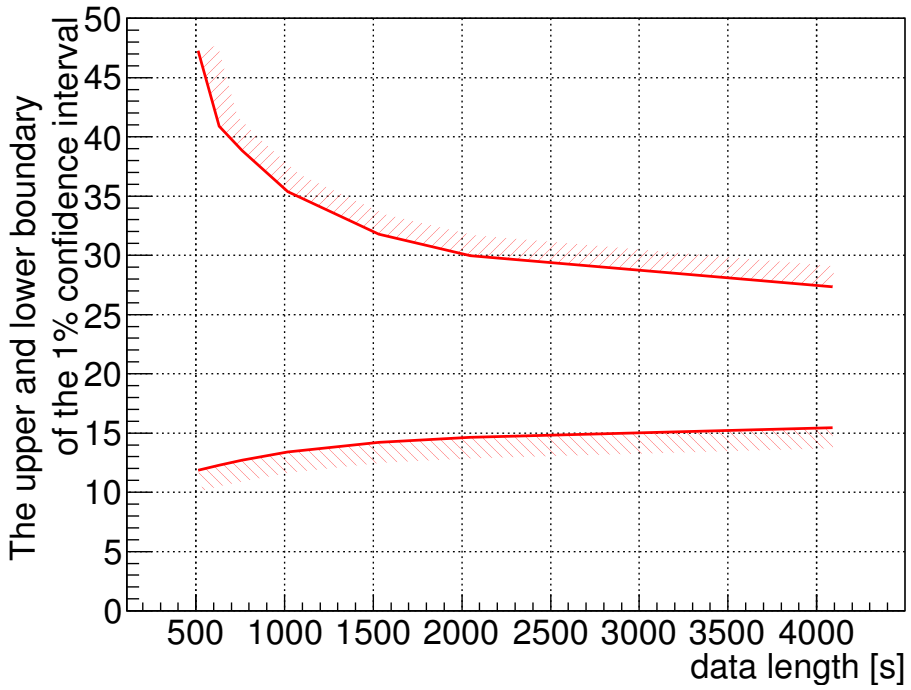

Figure 3.6: This plot shows the dependence of confidence interval as a function of the data length. The precision of the estimated ν is bad for short data.

3.4 Application to the real data

3.4.1 LIGO S5 observation data

We apply the above method to LIGO data of the fifth science run which can be obtained from the LIGO Open Science Center[39]. Fig. 3.7 shows the observed $\hat{\nu}$ at each frequency as a function of time. GPS time of the data is from 842747904 to 842760192, and the resolution of time δt and frequency δF are 128s, 16Hz, respectively. This result is obtained by the data length $T = 1024$s with overlapped time $T_{\rm lap} = 896$s.

The $\hat{\nu}$ in the frequency band 30-60Hz is ~ 15. The confidence interval is $9.3 \leq \hat{\nu} \leq 15.4$. This non-Gaussianity continues for 16384 seconds where we analyzed. The $\hat{\nu}$ in the frequency band 100-1kHz and the time 8000-9000s is ~ 50.

The threshold that the Gaussian hypothesis is rejected is 59 when $T = 1024$s from FIG. 3.3. The detector noise in the frequency band 30-60Hz can be regarded as non-Gaussian noise with 99% confidence. This domination of non-Gaussianity is consistent with the large deviation of the quantile from Gaussian noise shown in FIG. 2.2. The domination of non-Gaussianity in 8000-9000s is not revealed in FIG. 2.2. On the other hand, we can regard this time-frequency region as non-Gaussian noise with 99% confidence by using ν. FIG. 3.7 provides us with the temporal evolution of non-Gaussianity of data. So we can reveal the time scale in which the non-Gaussianity is dominant.

The domination of non-Gaussianity due to noise transient which appears around 8000s, from 100 to kHz band is detected. In this region, ν is from 40 to 60 and non-Gaussianity continues for about 300 seconds. This transient non-Gaussianity is also enough to reject the assumption that the detector noise in this region is Gaussian with 99% confidence(local probability).

These results show the detector noise can be distinguished from Gaussian noise quantitatively. In addition to this we succeed to extract the degree of non-Gaussianity in the time scale and frequency band.

Fig. 3.8 shows the distribution of the LIGO detector noise in the time-frequency region where the frequency and the time elapsed from the GPS time = 842747904 of red and blue histograms are (f = 128Hz, t = 6144s) and (f = 32Hz, t = 1024s), respectively. The estimated $\hat{\nu}$ of the former region is $\sim$ 200 which can be regarded as Gaussian. That of the latter region is $\sim$ 15 lasting entire time in the figure. The latter region is not Gaussian distributed and this non-Gaussianity is not transient but the stationary non-Gaussianity at least this noise behavior continues 16384s.

FIG. 3.9 shows the time evolution of the observed $\hat{\nu}$ at each frequency in GPS times different from FIG. 3.7. The GPS times of the first samples of those data sets are 841449472, 842489856, 864575488 and 870838272 with 16384 seconds long data. Other parameters are the same as those of FIG. 3.7. We have arbitrarily selected those four periods of data except for the selection conditions where those periods (1) do not contain any gap (i.e., no loss of

samples) for 18,000 seconds, (2) include no hardware injection, and (3) satisfy the "CAT1" in the literature of LIGO and Virgo collaboration[37]. Moreover, we demand that (4) those periods almost satisfy the "CAT3/4" conditions except for the one starting at the GPS time 870838272 where we intended to study the effect of "CAT4". "CAT" represents the data quality which is defined by LIGO and Virgo collaboration. According to [37], the data which does not satisfy the "CAT1" is excluded for science, because this data segment includes malfunctions of the detector. In the data segments which does not satisfy the "CAT3/4", the coupling between the noise and detector output is established. Note that we demand the condition (1) to exclude possible edge effects and used only middle 16,384 seconds of data. The deterioration of Gaussianity in low frequency band can be revealed in all figures. Bottom right panel shows $\hat{\nu}$ of the bad quality data where data does not belong to "CAT4". The Gaussianity of the data shown in bottom right panel of FIG. 3.9 can be rejected in almost all frequencies and time with 99% confidence. Four panels in FIG. 3.9 suggest that the domination of non-Gaussianity appears in the LIGO S5 data even though the data is categorized as "CAT4" which represents good quality enough for science.

3.4.2 iKAGRA observation data

The iKAGRA is the first observation phase of the KAGRA without cryogenic mirrors. The observations were taken place twice from 25 Mar. 2016 to 31

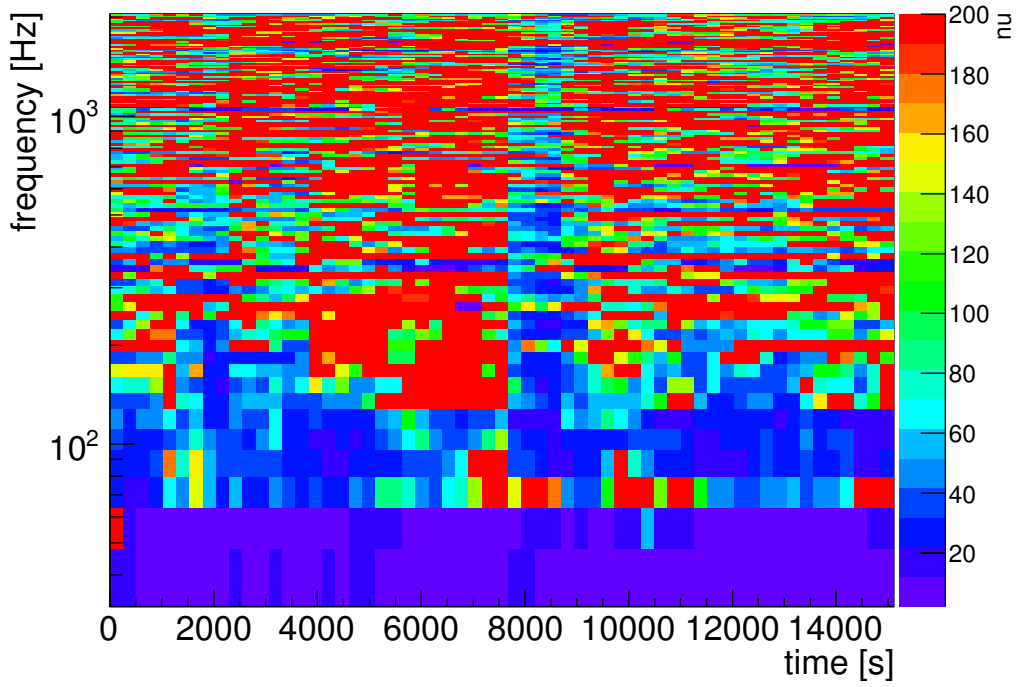

Figure 3.7: This plot shows the estimated $\hat{\nu}$ for the real LIGO S5 data as a function of time. GPS time of the data is from 842747904 to 842760192, resolution of time δt and frequency δF are 128s, 16Hz, respectively. This result is obtained by the data length $T = 1024$s with overlapped time $T_{\rm lap} = 896$s. Purple region means Gaussianity of noise is bad and there are many non-Gaussian region especially in low frequency band.

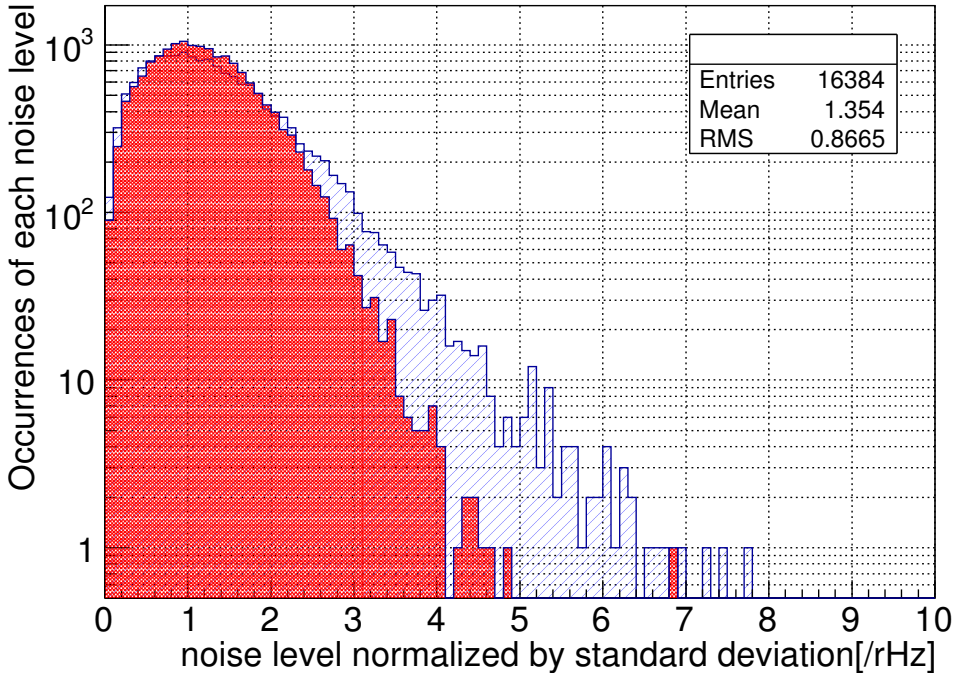

Figure 3.8: This plot shows the distributions of the LIGO detector noise in the time-frequency region where time from GPS=842747904, t, frequency, f, and their widths, dt, df are ($t = 6144$s, $f = 128$Hz, $dt = 128$s, $df = 16$Hz) for red histogram and ($t = 1024$s, $f = 32$Hz, $dt = 128$s, $df = 16$Hz) for blue one. Entry of each histogram is 16384.

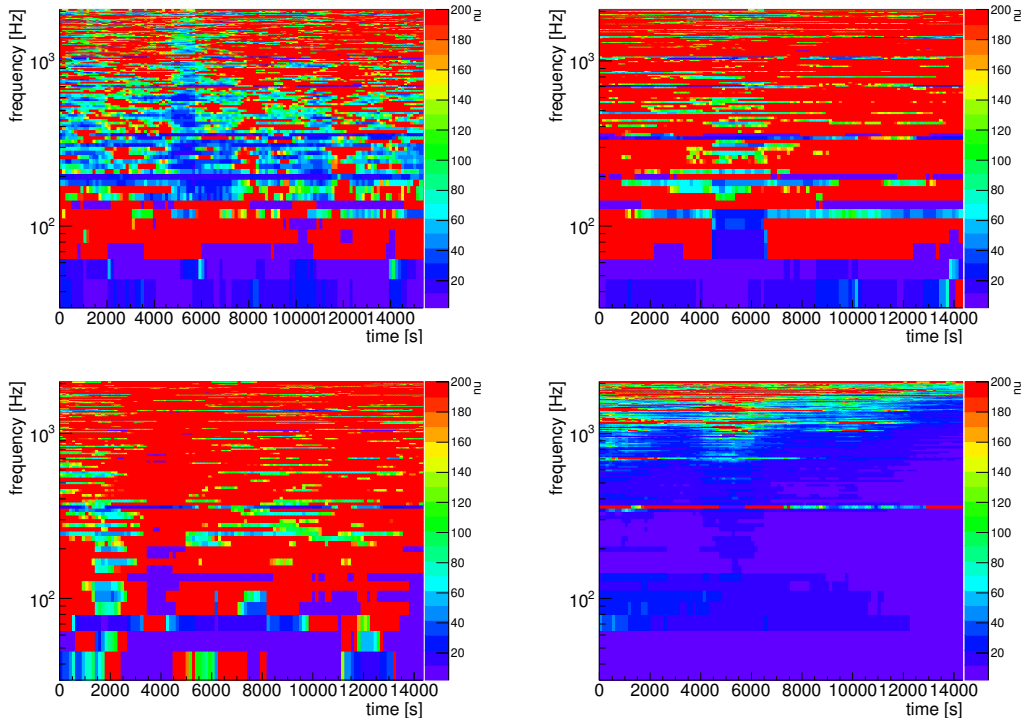

Figure 3.9: These plots show the time evolution of the observed $\hat{\nu}$ at each frequency of the LIGO S5 observational data. GPS time of the top left, the top right, the bottom left and the bottom right panel is 841449472, 842489856, 864575488 and 870838272, respectively. Other parameters are same as ones of FIG. 3.7. Bottom right panel shows the bad quality data which does not belong to "CAT4" in the literature of LIGO and Virgo collaboration[37]. Other panels show good quality data which belongs to "CAT4".

Mar. 2016 and from 11 Apr. 2016 to 25 Apr. 2016. The longest continuous lock was longer than 16 hours and the typical strain sensitivity was $\sim 10^{-15}$ at the 200Hz.

We apply our method for iKAGRA observational data and estimate $\nu(t, f)$ as a measure of non-Gaussianity. The $\nu(t, f)$ of the iKAGRA data is shown in FIG. 3.10. The analyzed four data segments are chosen from the longest uninterrupted lock. The GPS time of these segments are 1144320096, 1144561984, 1144706592 and 1144924256. Another parameters are same as those of FIG. 3.7.

Below 100Hz, the continuous non-Gaussianity can be seen common in the LIGO S5 observation data. The hypothesis that the detector noise follows Gaussian distribution is rejected with 99% confidence level in these time-frequency region.

Moreover the periodical occurrence of the non-Gaussianity can be seen around 1kHz. Those non-Gaussianities continue for about 1000s and their period are roughly 2 hours.

3.5 Robustness of ν for non-stationary noise

In the previous section, we assumed that the detector noise is stationary at least during the data length T. However the detector noise in many cases contains the non-stationary noise, and it is difficult to assume that the detector noise is completely stationary in long period such as one hour, one day, and so on.

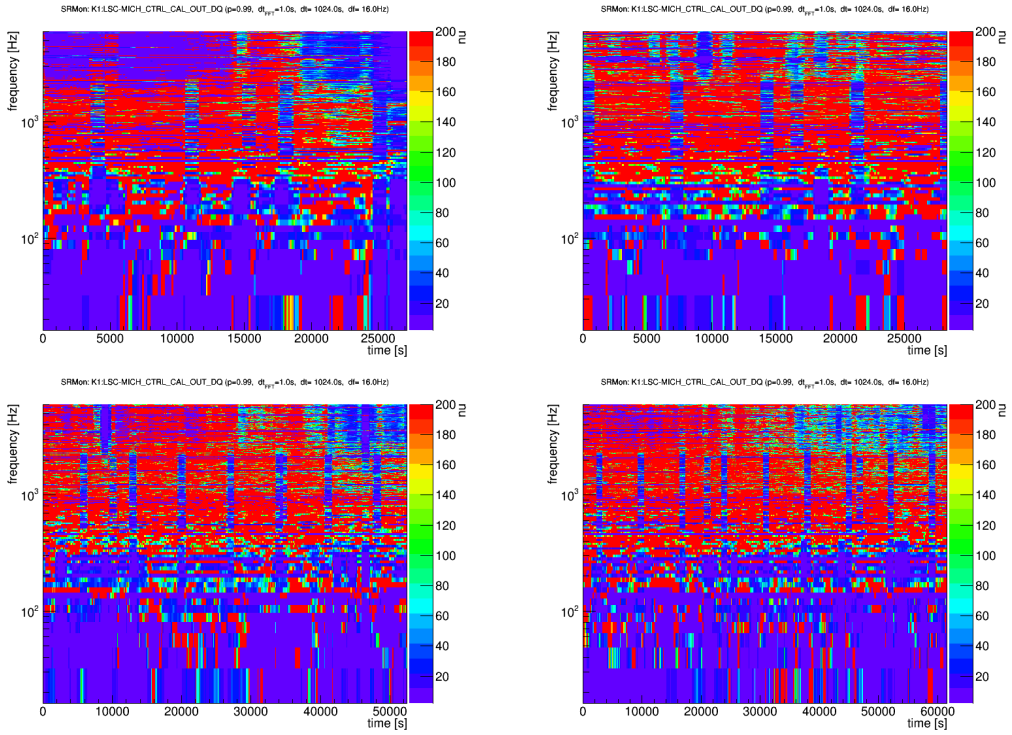

Figure 3.10: These plots show the time evolution of the observed $\hat{\nu}$ at each frequency of the iKAGRA observational data. GPS time of the top left, the top right, the bottom left and the bottom right panel is 1144320096, 1144561984, 1144706592 and 1144924256, respectively. Other parameters are same as ones of FIG. 3.7. In this configuration, the Gaussian hypothesis is rejected in $\nu_{\rm th} < 59.0$ with 99% confidence.

In order to investigate the effect of the non-stationary noise on our estimator ν, we apply our method for the simulated noise which contains (1) the stationary Gaussian noise, (2) the stationary Student-t noise, and (3) the stationary Gaussian noise with the non-stationary noise. The simulated noise in the case of (1) and (2) are the same as the Sec. 3.2, and Sec. 3.3, respectively. The simulated noise in the case of (3) contains the non-stationary noise whose amplitude corresponds to 5σ of the stationary Gaussian noise at the rate of one event per one minute.

Moreover we evaluated the kurtosis of the these three types of the simulated noises. The kurtosis is expected to be more sensitive by the non-stationary noise than the our estimator ν. We adopt the kurtosis whose expected value equals to zero in Gaussian noise

$$(\text{kurtosis}) = \frac{\frac{1}{N}\sum_{i=1}^{N}(x_i - \mu)^4}{\sigma^4} - 3, \tag{3.10}$$

where x_i is the samples, μ is the mean of x_i, and σ is the standard deviation of x_i.

The FIG. 3.11 shows the scatter plot of ν and kurtosis of the simulated noise with 4096s length. In the case of the stationary Gaussian and Student-t noise model, the relation between the ν and kurtosis is given as

$$(\text{kurtosis}) = \frac{6}{\nu - 4}. \tag{3.11}$$

The kurtosis is monotonic increasing with decreasing ν in the stationary noise cases.

On the other hand, the existence of the non-stationary noise does not affects the estimated ν, although the estimated kurtosis increase by the existence of the non-stationary noise.

We conclude that ν can be used as more robust indicator for evaluating stationary non-Gaussianity than kurtosis.

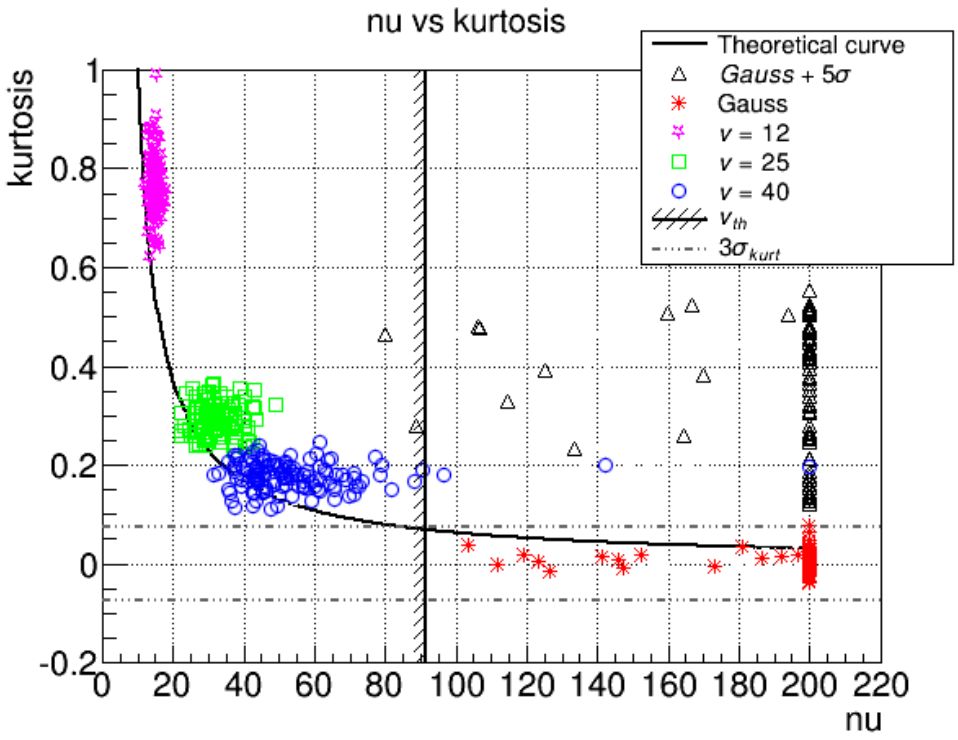

Figure 3.11: This plot shows the estimated ν and kurtosis of the simulated noise. The red asterisk, blue circles, green square, pink stars, and black triangles represent the ν and kurtosis of the Gaussian noise, the Student-t noise with $\nu = 40$, one with $\nu = 25$, one with $\nu = 12$, and the Gaussian noise with the non-stationary noise with the 4096s length. The amplitude of the stationary noise corresponds the 5σ of the one of the Gaussian noise, and the rate of the non-stationary noise is one event per one minute. The solid line represents the $\nu_{\rm th}$ which is calculated in the Sec. 3.2. The dashed line represents the expected value of 3σ of the kurtosis of the stationary Gaussian noise consist of N-samples. In this figure, each point is calculated from 65536 samples of $\tilde{n}(f)$.

Chapter 4

Search Method of Compact Binary Coalescence Event

4.1 Optimal filtering

In this section, we denote the time series signal of detector output $s(t)$ as

$$s(t) = h(t) + n(t) \tag{4.1}$$

where $h(t)$ is a gravitational wave strain signal and $n(t)$ is a detector noise.

The waveform of GWs emitted from compact binary coalescence events can be calculated by using the post-Newtonian approximation. When the waveform of $h(t)$ is known, a simple method described in

$$\frac{1}{T}\int_0^T s(t)h(t)\mathrm{d}t = \frac{1}{T}\int_0^T h^2(t)\mathrm{d}t + \frac{1}{T}\int_0^T n(t)h(t)\mathrm{d}t, \tag{4.2}$$

where T is observation time, can be used for extracting the signal from the noise. We can detect $h(t)$ because the second term of Eq. (4.2) equals zero in

the limit of $T \to \infty$. So $h(t)$ can be used as a filter for searching signals buried in noise.

We discuss the optimal filter by maximizing signal-to-noise ratio in the case when the waveform is known. We consider

$$\mathcal{S} = \int_{-\infty}^{\infty} s(t)K(t)\mathrm{d}t, \tag{4.3}$$

where $K(t)$ is the optimal filter which should be determined. The signal-to-noise ratio is defined as the ratio of expected value of $\mathcal{S}$, when signal is present, S and the root-mean-square value of s when the signal is absent, N. Because $\langle n(t)\rangle = 0$, S and N become

$$\begin{aligned} S &= \int_{-\infty}^{\infty} \langle s(t)\rangle K(t)\mathrm{d}t & (4.4)\\ &= \int_{-\infty}^{\infty} h(t)K(t)\mathrm{d}t & (4.5)\\ &= \int_{-\infty}^{\infty} \tilde{h}(f)K^*(f)\mathrm{d}f, & (4.6) \end{aligned}$$

and

$$\begin{aligned} N^2 &= \int_{-\infty}^{\infty} \langle n(t)n(t')\rangle K(t)K(t')\mathrm{d}t\mathrm{d}t' & (4.7)\\ &= \int\int_{-\infty}^{\infty} \left(\int\int_{-\infty}^{\infty} \langle n(f)n(f')\rangle \mathrm{e}^{2\pi i(ft-f't')}\mathrm{d}f\mathrm{d}f' \right) K(t)K(t')\mathrm{d}t\mathrm{d}t' & (4.8)\\ &= \int_{-\infty}^{\infty} \frac{1}{2} S_n(f)|\tilde{K}(f)|^2, & (4.9) \end{aligned}$$

, where $S_{\mathrm{n}}(f)$ is the expected value of noise power spectrum.

We define

$$(x|y) = \int_{-\infty}^{\infty} \frac{\tilde{x}(f)\tilde{y}^*(f)}{(1/2)S_n(f)}\mathrm{d}f. \tag{4.10}$$

The signal-to-noise ratio, S/N is given as

$$\frac{S}{N} = \frac{(u|h)}{(u|u)^{1/2}}, \tag{4.11}$$

where u is defined as

$$\tilde{u}(f) = \frac{1}{2} S_n(f) \tilde{K}(f). \tag{4.12}$$

When the signal-to-noise ratio is maximized, h and $u/(u/u)^{1/2}$ should be parallel. Thus, $\tilde{u}(f)$ is proportional to $\tilde{h}(f)$. The filter $\tilde{K}(f)$ is determined as

$$\tilde{K}(f) = A \frac{\tilde{h}(f)}{S_n(f)}, \tag{4.13}$$

where A is the arbitrary constant. The matched filter is defined by Eq. (4.13). By using Eq. (4.11) ,(4.12) and (4.13), optimal value of signal-to-noise ratio is given as

$$\frac{S}{N} = (h|h)^{1/2} \tag{4.14}$$

and

$$\left(\frac{S}{N}\right)^2 = (h|h) \tag{4.15}$$

$$= 2 \int_{-\infty}^{\infty} \frac{|\tilde{h}(f)|^2}{S_n(f)} \tag{4.16}$$

$$= 4 \int_{0}^{\infty} \frac{|\tilde{h}(f)|^2}{S_n(f)}. \tag{4.17}$$

When the detector noise is white noise, $S_n(f)$ is constant, and the optimal filter is the gravitational wave strain h itself. On the other hand, when the detector noise is colored noise, Eq. (4.13) suggests that we should give a weight to the contribution to signal-to-noise ratio from the frequency region where the detector noise is noisy.

4.1.1 maximum likelihood

The likelihood function for the Gaussian noise can be described as

$$p_G(s|\theta) \propto \exp\left(-\frac{1}{2}\sum_j \frac{|s(f_j) - h_\theta(f_j)|^2}{S_n(f_j)}\right), \tag{4.18}$$

where θ is the parameter vector such as the two masses, m_1 and m_2, of binary.

The likelihood ratio between the cases of the presence and the absence of gravitational waves is given as

$$\begin{aligned} \Lambda_G(s) &= \frac{p_G(s|\theta)}{p_G(s|0)} \\ &= \frac{\exp\left(-\frac{1}{2}\sum_j \frac{|s(f_j)-h_\theta(f_j)|^2}{S_n(f_j)}\right)}{\exp\left(-\frac{1}{2}\sum_j \frac{|s(f_j)|^2}{S_n(f_j)}\right)} \\ -2\log(\Lambda_G(s)) &= \sum_j \frac{|s(f_j) - h_\theta(f_j)|^2}{S_n(f_j)} - \sum_j \frac{|s(f_j)|^2}{S_n(f_j)} \end{aligned} \tag{4.19}$$

Now, we consider to maximize likelihood ratio. The Gaussian likelihood ration is rewritten by using the notation of inner product in

$$\log(\Lambda(s)) = \log\left(\frac{\exp[-\frac{1}{2}(s-h|s-h)]}{\exp[-\frac{1}{2}(s|s)]}\right) \tag{4.20}$$

$$= -\frac{1}{2}(s-h|s-h) + \frac{1}{2}(s|s) \tag{4.21}$$

$$= (s|h) - \frac{1}{2}(h|h). \tag{4.22}$$

When we set the inner product of template waveform each other, $(h|h)$, to be H^2 and set h/H to be $\hat{h}$,

$$\log(\Lambda(s)) = H(s|\hat{h}) - \frac{1}{2}H^2 \tag{4.23}$$

and

$$\max_H \log(\Lambda(s)) = \frac{1}{2}(s|h)^2. \tag{4.24}$$

By the above, maximizing Gaussian likelihood ratio is equivalent to compute the square of the matched filter output.

In the next section, we discuss to modify the filter which is optimal under the Gaussian noise environment for the non-Gaussian noise environment.

4.2 Non-Gaussian Filter

The matched filtering and the Gaussian likelihood function are optimal to search for gravitational waves under the Gaussian noise background. However, the non-Gaussianity may dominate in a certain time and frequency region such as in FIG. 3.9. When the detector noise is not Gaussian, the matched filtering method is not an optimal method.

It is difficult to modify the matched filtering method for non-Gaussian noise, because the noise distribution does not explicitly appear in the matched filtering formula. On the other hand, the likelihood function contains the Gaussian distribution function explicitly. So we can construct the likelihood function for various noise distributions when the distribution of the detector noise is known.

We proposed a method for evaluating non-Gaussianity in Chap. 3. Our method can provide ν as an indicator of the non-Gaussianity which is the parameter of the Student-t distribution. The indicator ν can ensure that the Student-t distribution is better approximation of the noise distribution than the Gaussian distribution because Student-t distribution contains the Gaussian

distribution as the limit of $\nu \to \infty$.

When the detector noise follows Student-t distribution, the likelihood function is modified. According to Eq. (2.6), the likelihood function for the Student-t noise can be described as

$$p_{ST}(s|\theta) \propto \exp\left(-\sum_j \frac{\nu(f_j)+2}{2}\log\left[1+\frac{1}{\nu(f_j)}\frac{|s(f_j)-h_\theta(f_j)|^2}{S_{\rm n}(f_j)}\right]\right). \quad (4.25)$$

Then the log likelihood ratio between the presence and the absence of the gravitational wave is given as

$$\begin{aligned}\log(\Lambda_{ST}(s)) &= \log\left(\frac{p_{ST}(s|\theta)}{p_{ST}(s|0)}\right) \\ &= \sum_j \frac{\nu(f_j)+2}{2}\log\left(\frac{1+\frac{1}{\nu(f_j)}\frac{|s(f_j)|^2}{S_{\rm n}(f_j)}}{1+\frac{1}{\nu(f_j)}\frac{|s(f_j)-h_\theta(f_j)|^2}{S_{\rm n}(f_j)}}\right). \quad (4.26)\end{aligned}$$

Student-t likelihood function is also optimal for the Gaussian noise because the Student-t distribution include the Gaussian distribution at the limit of $\nu \to \infty$. The Student-t likelihood function is expected to be optimal even in the case of the Gaussian noise by giving large enough ν.

We adopt Eq. (4.26) as a new detection statistic instead of Eq. (4.11) and (4.19).

Chapter 5

Pragmatic study of search algorithm

5.1 Data Setup

We investigate the Student-t likelihood function in the case of the Student-t noise environment..

5.1.1 Simulated noise

In order to investigate the response of the Student-t likelihood function to the Gaussian noise, we generated and used the simulated Gaussian and Student-t noise whose expected value of power spectrum follows the KAGRA design sensitivity.

When the real pert, $\Re[\tilde{n}(f)]$, and imaginary part, $\Im[\tilde{n}(f)]$, of the noise

spectrum are independent each other, the relation between the design sensitivity, $S_n(f)$, and the standard deviation, $\sigma_{\Re}$ and $\sigma_{\Im}$ of the simulated Gaussian noise, $\tilde{n}(f)$ can be described as

$$S_n(f) = \frac{\sigma^2_{\Re}(f) + \sigma^2_{\Im}(f)}{T}, \tag{5.1}$$

where T is the data length for estimating $S_n(f)$, and we assumed that the mean of the $\Re[\tilde{n}(f)]$ and $\Im[\tilde{n}(f)]$ equal zero. When $\Re[\tilde{n}(f)]$ and $\Im[\tilde{n}(f)]$ are independent each other and follow same distribution, $S_n(f)$ can be rewritten as

$$S_n(f) = \begin{cases} \dfrac{2}{T}\sigma^2 & \cdots \quad \text{(for Gaussian)} \\ \dfrac{2}{T}\dfrac{\nu}{\nu-2}\sigma_s^2 & \cdots \quad \text{(for Student-t)} \end{cases}, \tag{5.2}$$

where σ, σ_s, and ν are defined in Eq. (2.4) and (2.8). Generated simulation noise spectrum of the Gaussian and Student-t noise are shown in FIG. 5.1. The suspension lines are excluded from the design sensitivity curve for simplification. The frequency regions where the lines are excluded are interpolate by linear interpolation method.

5.1.2 GW150914

Two advanced LIGO detected GW from the coalescence of a binary black hole whose masses are $38.8M_{\odot}$ and $31.6M_{\odot}$. The 4096-second of data around GW150914 is made public and shown in FIG. 5.2. The top panel and bottom panel represent the time series of detector output of LIGO Hanford and Livingston, respectively. The averaged power spectrum of these time series signals

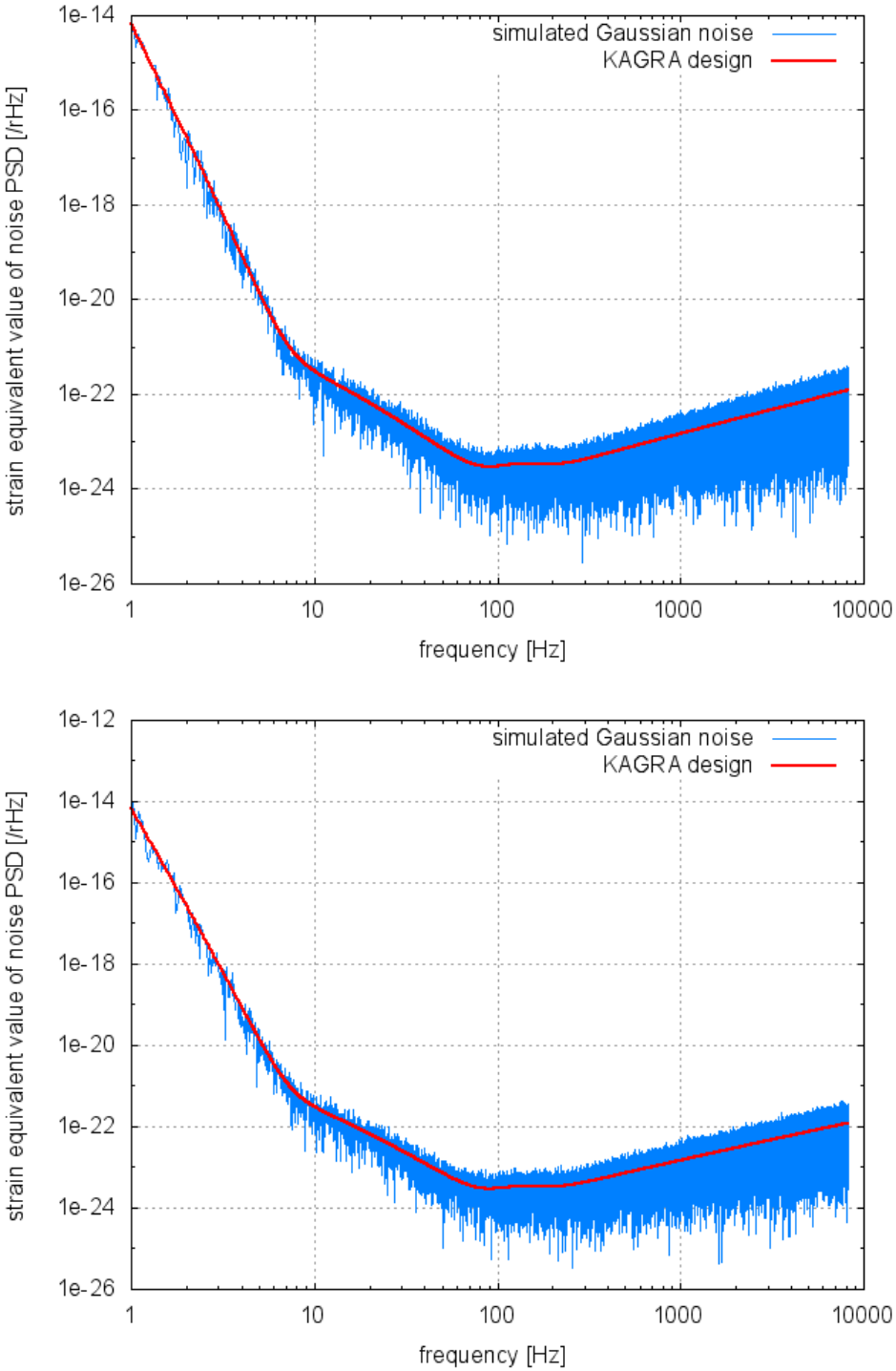

Figure 5.1: The top and bottom panel shows the simulated noise power spectrum of Gaussian noise and the Student-t noise with $\nu = 25$. Both noise spectrums follow the KAGRA design sensitivity curve(red solid line). For simplification, the suspension lines are excluded from the sensitivity curve.

is shown in FIG. 5.3. The data length for the fast Fourier transform t_{FFT} is 1s and averaged number is 4096. The strain sensitivity is several times of 10^{-24} in the most sensitive region around 200Hz. The low frequency region below 10Hz can not be used to search for gravitational waves because this region is cut off by the high pass filter to ensure the dynamic range of the detector signals.

These data are analyzed, and the non-Gaussianity and the time evolution of ν of these data are obtained. The results are shown in FIG. 5.4. The time and frequency resolution of this figure are 16s and 16Hz, respectively. The data length T for estimating ν and quantile p are 512s and 0.99, respectively. When $T = 512$, the threshold that the Gaussian hypothesis is rejected is $\nu_{\mathrm{th}} = 45$ with 99% confidence level. We find that the non-Gaussianity is dominant mainly in low frequency region.

Strictly speaking, we must estimate ν of the detector noise by taking into account of the gravitational wave signal because the existence of the gravitational wave around 2048s in FIG. 5.2 and 5.4 is already known. The robustness of ν against the non-stationary noise was investigated in Sec. 3.5. The duration of the GW150914 event which was detected by advanced LIGO is no more than one second, and only one gravitational wave event is known to exist in the 4096s data. The effect of the gravitational wave signal on the estimated ν is thus negligible. When we detect the gravitational waves with large signal-to-noise ratio which last for hundreds seconds such like gravitational waves from binary neutron stars, we should consider the effect of the gravitational

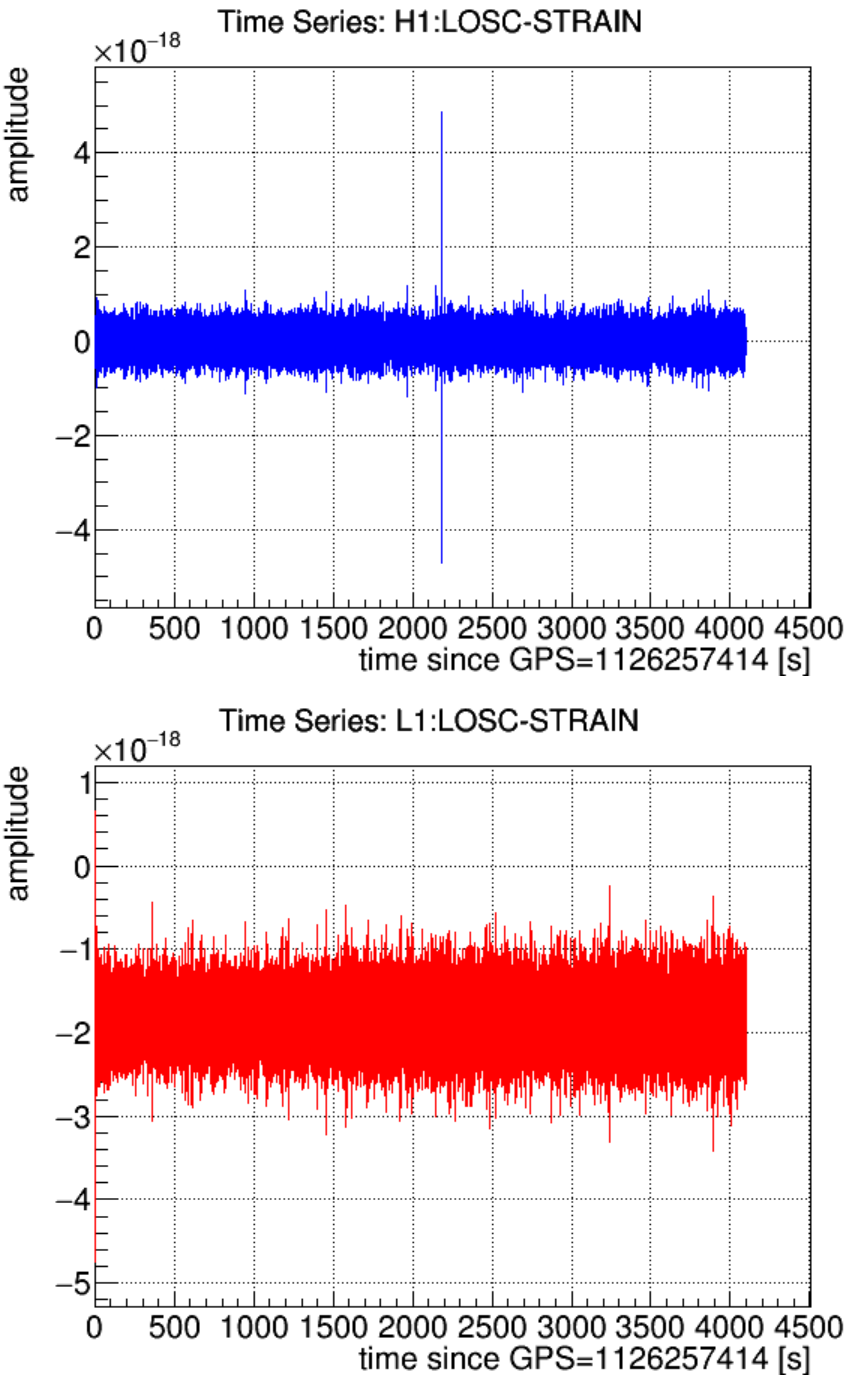

Figure 5.2: This plot shows the time series of the strain equivalent signal of LIGO Hanford(top panel) and LIGO Livingston(bottom panel).

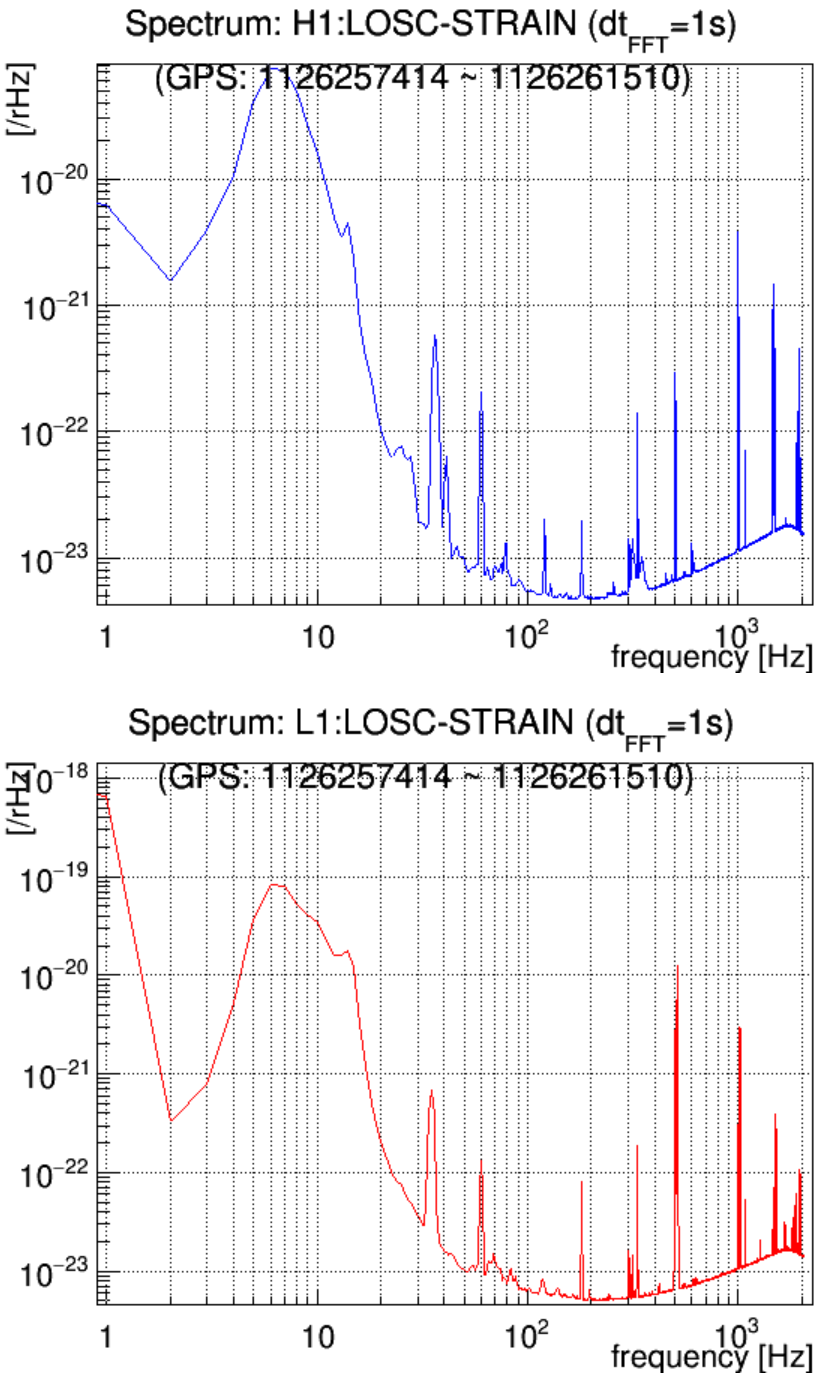

Figure 5.3: This plot represent the averaged power spectrum of the FIG. 5.2.

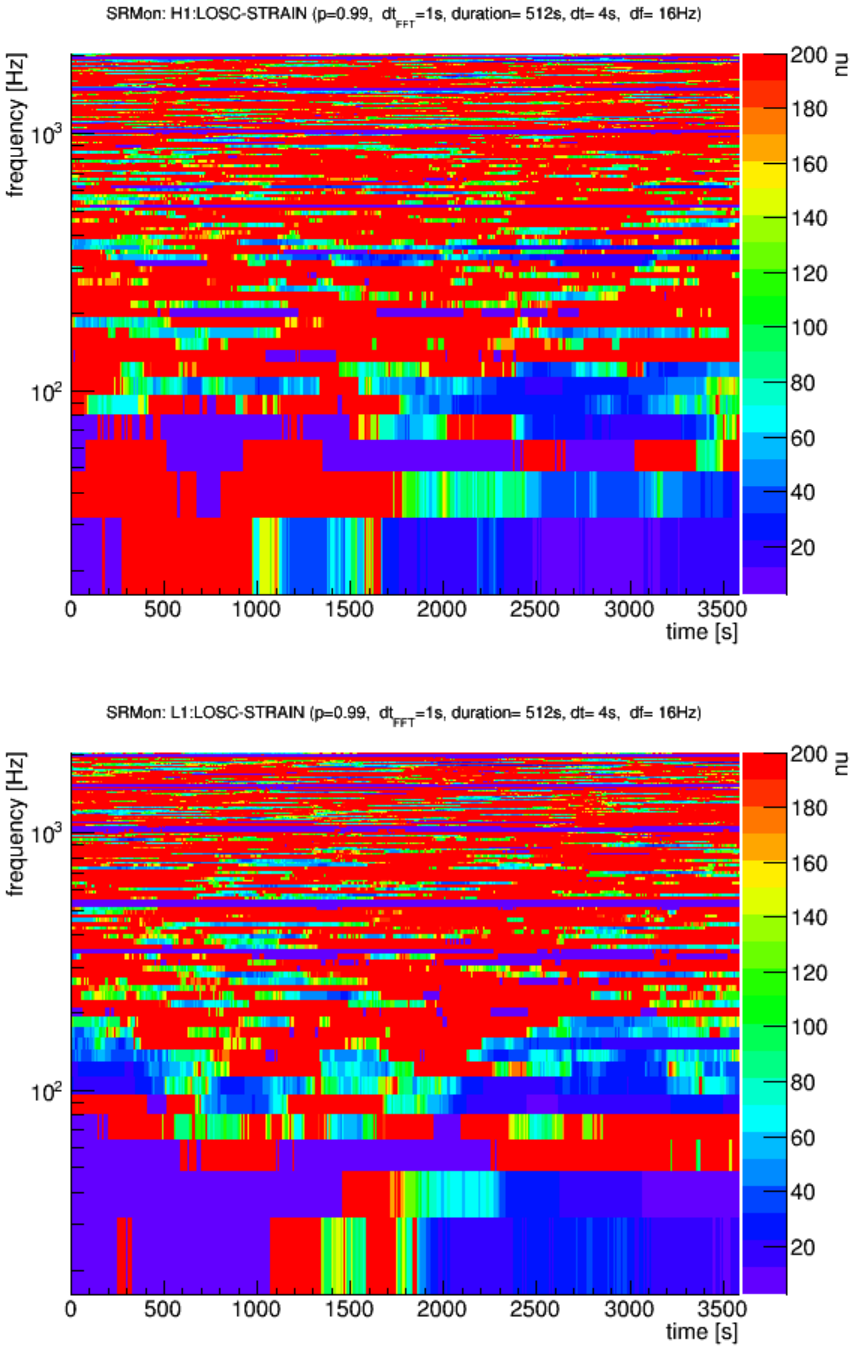

Figure 5.4: The time evolution of the estimated ν of LIGO Hanford(top panel) and LIGO Livingston(bottom panel). In both panels, the domination of the non-Gaussianity can be seen in the low frequency band. The threshold which reject the hypothesis that the detector noise is Gaussian is $\nu_{\rm th} = 45$.

wave signal on the estimation of ν.

5.1.3 Template Waveform

In order to demonstrate the optimal filter for non-Gaussian noise, we employ the waveforms called post-Newtonian waveform whose masses are $38.8M_\odot$ and $31.6M_\odot$. These masses are same value as the masses of the GW150914 event obtained by LIGO and Virgo collaboration. [14].

The post-Newtonian waveform is described as

$$h_+(f) = \frac{1+\cos^2\iota}{2}\left(\frac{5\pi}{24}\right)^{1/2}\eta^{1/2}\frac{G^2M^2}{c^5r}x^{-7/4}e^{-2\pi i f t_c}e^{2\pi i\phi_c}e^{-i\Psi(f)} \quad (5.3)$$

$$h_\times(f) = i\cos\iota\left(\frac{5\pi}{24}\right)^{1/2}\eta^{1/2}\frac{G^2M^2}{c^5r}x^{-7/4}e^{-2\pi i f t_c}e^{2\pi i\phi_c}e^{-i\Psi(f)} \quad (5.4)$$

where ι is the inclination angle, $\eta = \frac{m_1m_2}{(m_1+m_2)^2}$ is the symmetric mass ratio, G is the gravitational constant, M is the total mass, c is the speed of light, $x = (\pi GMf/c^3)^{2/3}$, t_c is the coalescence time, ϕ_c is the phase at t_c, and $\Psi(f)$ is given as

$$\begin{aligned}\Psi(f) = &- \frac{\pi}{4} + \frac{3}{128}\frac{1}{\eta}x^{-5/2}\left\{1+\left(\frac{3715}{756}+\frac{55}{9}\eta\right)x - 16\pi x^{3/2}\right.\\
&+ \left(\frac{15293365}{508032}+\frac{27145}{504}\eta+\frac{3085}{72}\eta^2\right)x^2\\
&+ \left(\frac{38645}{756}-\frac{65}{9}\eta\right)\left[1+\frac{3}{2}\ln\left(\frac{x}{x_0}\right)\right]\pi x^{5/2}\\
&+ \left[\frac{11583231236531}{4694215680}-\frac{640}{3}\pi^2-\frac{6848}{21}\gamma_E-\frac{3424}{21}\ln(16x)\right.\\
&\quad \left.+\left(-\frac{15737765635}{3048192}+\frac{2255}{12}\pi^2\right)\eta+\frac{76055}{1728}\eta^2-\frac{127825}{1296}\eta^3\right]x^3\\
&+ \left.\left(\frac{77096675}{254016}+\frac{378515}{1512}\eta-\frac{74045}{756}\eta^2\right)\pi x^{7/2}\right\}, \quad (5.5)\end{aligned}$$

where γ_E is Euler-Mascheroni constant.

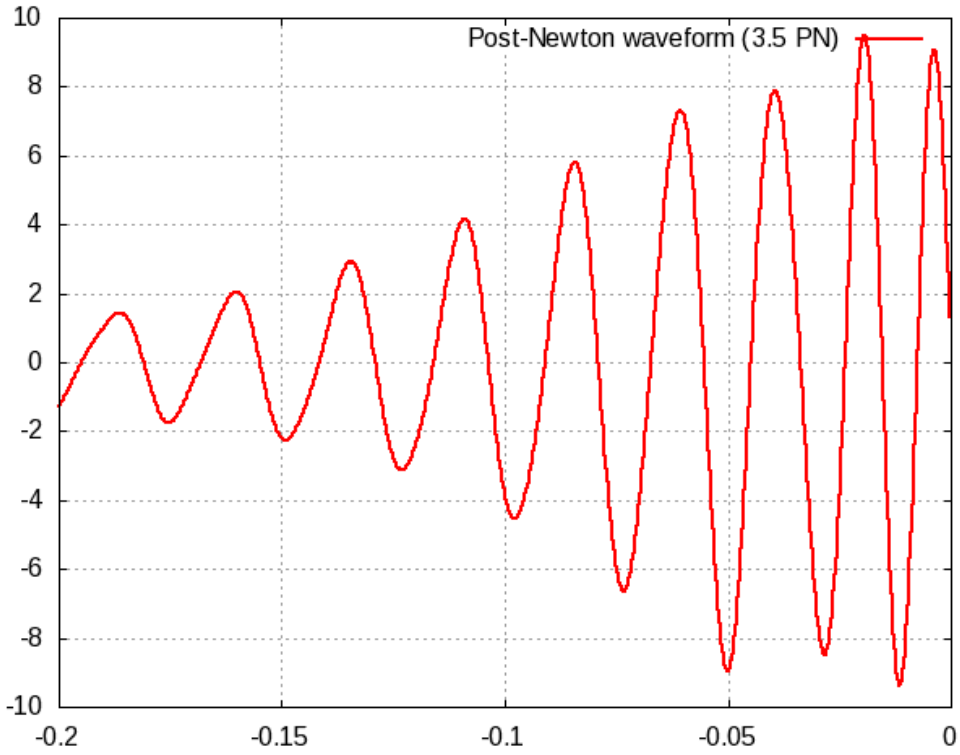

Figure 5.5: This figure shows the 3.5 order Post-Newtonian waveform from the binary system whose masses are $38.8M_{\odot}$ and $31.6M_{\odot}$. This waveform includes the frequency components from 37Hz to 64.3Hz.

FIG. 5.5 shows the 3.5 ordered post-Newtonian waveform from the binary system whose masses are $38.8M_{\odot}$ and $31.6M_{\odot}$. This time series waveform is generated by the inverse Fourier transform of the Eq. (5.3), (5.4) and (5.5), and includes frequency components from 37Hz to 64.3Hz.

5.1.4 Optimal filter configuration

In order to demonstrate the filter which is optimized for Student-t noise model, the time evolution of the filter output $\rho(t)$ is calculated with the advanced

LIGO observational data which includes GW150914. The $\rho(t)$ is calculated as

$$\rho(t) = \Lambda(s(f)e^{2\pi i f t}) \tag{5.6}$$

where $s(f)$ is the spectrum of the detector output and Λ is defined in Sec. 4.2.

The upper and lower frequency of the template waveform and the integration frequency range of the optimal filters should be limited when we apply the optimal filter. The upper frequency is decided from the frequency at the coalescence time , because the Post-Newtonian waveform is contains only inspiral phase. When the masses of binary are $38.8M_{\odot}$ and $31.6M_{\odot}$, the frequency at the coalescence time is 64.3Hz. The lower frequency is decided from the power spectrum of the detector noises. The power spectrum of the LIGO detectors noise whose frequency region is from 30Hz to 65Hz are shown in FIG.5.6.

In the noise of both detector, there are the loud line noise around 35Hz. Moreover the contribution of the low frequency band to signal-to-noise ratio is expected to be smaller than the that of the a few hundred Hertz band because the detector noise is rapidly increasing at the low frequency region(see FIG. 5.3). We adopt the lowest frequency of the template waveform as 37Hz in order to avoid the loud line. So the frequency band of the our optimal filter is from 37Hz to 64.3Hz. There also are another loud lines around 41Hz(Hanford only), 46Hz(Hanford only), and 60Hz(Hanford and Livingston). For simplicity, we exclude 1Hz-width around these loud line noise from the integration of the optimal filter though the line noise should be removed after considering the central frequency, amplitude, and Q-value for earning signal-to-noise ratio.

The duration of the template waveform we generated is about 0.15s. $\rho(t)$ is computed by using 32 seconds of data and template waveform with zero padding. For excluding possible edge effects, the data is overlapped for 16 seconds and only the middle 16 seconds of the calculated $\rho(t)$ are used. The schematic picture of the data flow is shown in FIG. 5.7.

5.2 Event Candidate

5.2.1 simulated Gaussian noise

In order to investigate that the response for the stationary Gaussian noise of the Student-t filter is same as one of the Matched filter, we apply the Student-t filter and Gaussian matched filter for the simulated Gaussian noise which is explained in Sec. 5.1.1.

The output, $\rho(t)$, of the Gaussian matched filter and the Student-t likelihood ratio for the simulated Gaussian noise are shown in FIG. 5.8. In order to compare the $\rho(t)$ of the Gaussian and Student-t filter, we normalize $\rho(t)$ as

$$\hat{\rho}(t) = \frac{\rho(t) - \mu_\rho}{\sigma_\rho}, \tag{5.7}$$

where μ_ρ and σ_ρ are the mean and standard deviation of the $\rho(t)$, respectively. The difference of the normalized output of the Gaussian filter, $\rho_{\rm G}(t)$, and Student-t filter, $\rho_{\rm ST}(t)$ is defined as

$$\rho_{\rm diff}(t) = \hat{\rho}_{\rm ST}(t) - \hat{\rho}_{\rm G}(t) \tag{5.8}$$

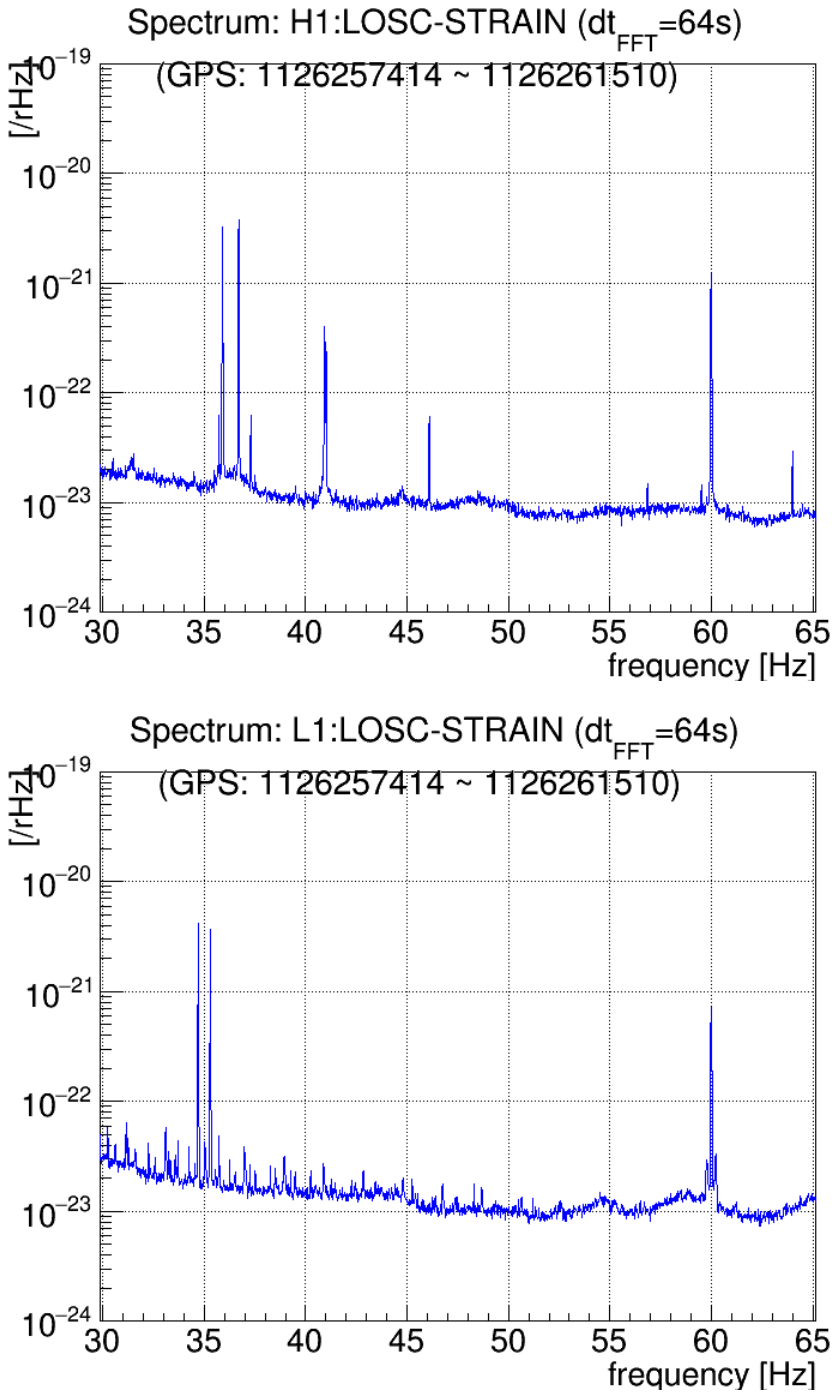

Figure 5.6: This plot shows the noise power spectrum of LIGO Hanford(top panel) and Livingston(bottom panel) whose frequency region is from 30Hz to 65Hz. There are the loud lines around 30Hz and 60Hz in the data of both detectors. In the data of Hanford, there are the loud lines around 41Hz and 46Hz. These loud lines exclude the integration of matched filter and non-Gaussian filter because the loud noise decrease signal-to-noise ratio of gravitational wave events.

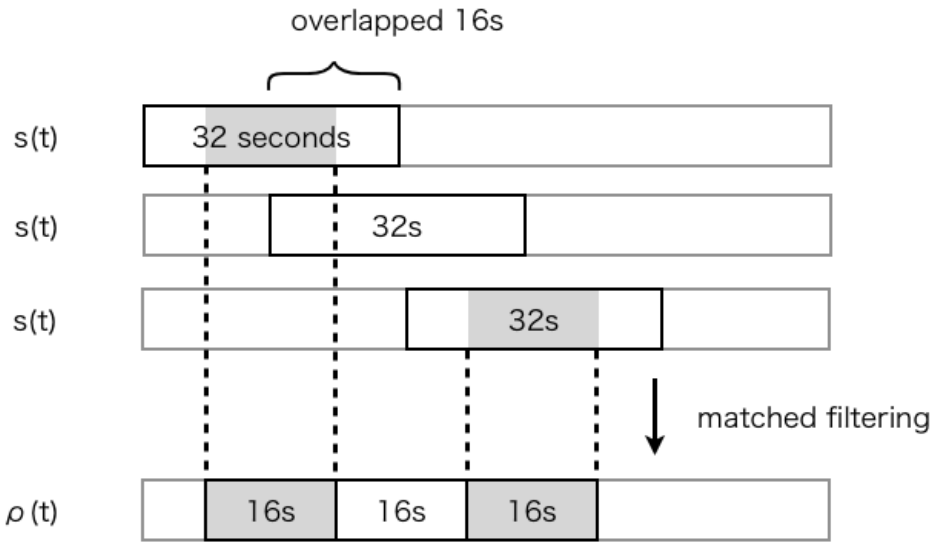

Figure 5.7: The schematic of the time shifted matched filtering

and is shown in FIG. 5.9. The $\rho_{\rm diff}$ follows a Gaussian distribution whose mean and standard deviation are -1.11×10^{-8} and 3.83×10^{-5}, respectively. The detection threshold is often set as $\rho = 8$ or 10. From the above, the difference between the $\rho_{\rm ST}$ and $\rho_{\rm G}$ is small enough than the detection threshold. Thus, the Student-t filter can be used instead of the Gaussian filter even though the detector noise follows a Gaussian distribution.

5.2.2 Simulated Student-t noise

In order to compare the detection efficiency for the non-Gaussian noise of Student-t filter with one of the Gaussian matched filter, we apply the Student-t filter and Gaussian matched filter for the simulated Student-t noise with $\nu = 25$. The filter output is computed for Student-t noise, $\rho_{\rm noise}$, and injected

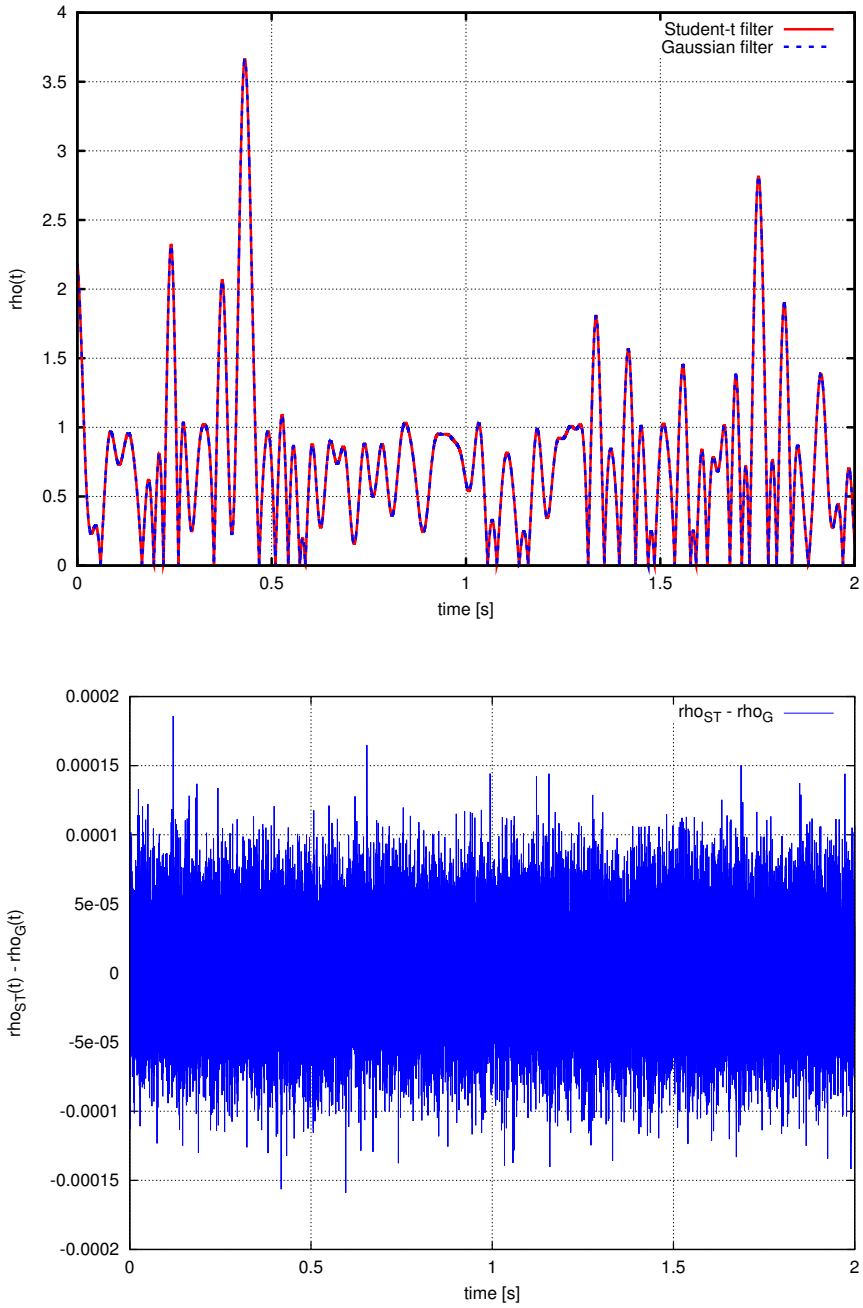

Figure 5.8: The top panel shows the normalized likelihood ratio $\hat{\rho}(t)$ for the simulated Gaussian noise which follows the KAGRA design sensitivity shown in FIG. 1.5. Red solid line and blue dashed line represent $\hat{\rho}(t)$ of the Student-t filter and Gaussian filter, respectively. The bottom panel shows the $\hat{\rho}_{\rm ST}(t) - \hat{\rho}_{\rm G}(t)$.

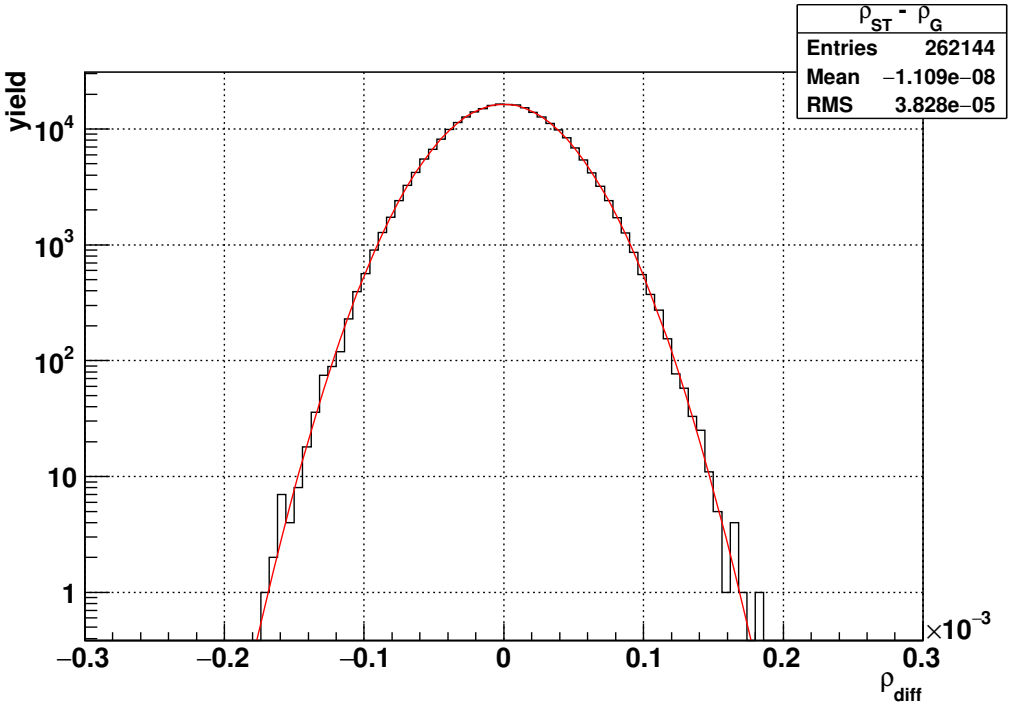

Figure 5.9: This plot shows the histogram of the residual of ρ_{ST} and ρ_{G}. The sample number of the histogram is 262144. The residual follows the Gaussian distribution whose mean and standard deviation are -1.11×10^{-8} and 3.83×10^{-5}, respectively. The residual of ρ_{ST} and ρ_{G} is small enough because Student-t filter involve the Gaussian filter as $\nu \to \infty$

gravitational wave signals from binary systems which is explained in Sec. 5.1.3, $\rho_{\rm gw}$.

The top panel and bottom panel of FIG. 5.10 show the histograms of output, ρ, of the Student-t filter and Matched filter, respectively. In both panel, the blue histogram and the red histogram represent the $\rho_{\rm noise}$ and $\rho_{\rm gw}$, respectively. The entry numbers of the histogram are 261120 (for $\rho_{\rm noise}$) and 1024 (for $\rho_{\rm gw}$ and the expected signal-to-noise ratio of injected signal is equal to 3.

The receiver operating characteristic curve can be computed from the FIG. 5.10 When we set the detection threshold as $\rho_{\rm th}$, the false alarm rate and detection efficiency can be defined as

$$p_{\rm far}(\rho_{\rm th}) = N_{\rho_{\rm noise}\leq\rho_{\rm th}}/N_{\rm noise}, \tag{5.9}$$

and

$$p_{\rm eff}(\rho_{\rm th}) = N_{\rho_{\rm gw}\leq\rho_{\rm th}}/N_{\rm gw}, \tag{5.10}$$

where $N_{\rho_{\rm noise}\leq\rho_{\rm th}}$ and $N_{\rho_{\rm gw}\leq\rho_{\rm th}}$ represent the number of greater than $\rho_{\rm th}$ out of $\rho_{\rm noise}$ and $\rho_{\rm gw}$, respectively, and $N_{\rm noise}$ and $N_{\rm gw}$ are the entry number of the blue and red histogram, respectively.

In FIG. 5.11, the blue and red solid line represents the receiver operating characteristic curve of Student-t filter and Matched filter respectively. Black solid line shows the difference between the detection efficiency of Student-t filter and one of the Gaussian matched filter at the same false alarm rate. The Student-t filter provides more than 1%-improvement of the detection efficiency at 1e-4 of the false alarm rate.

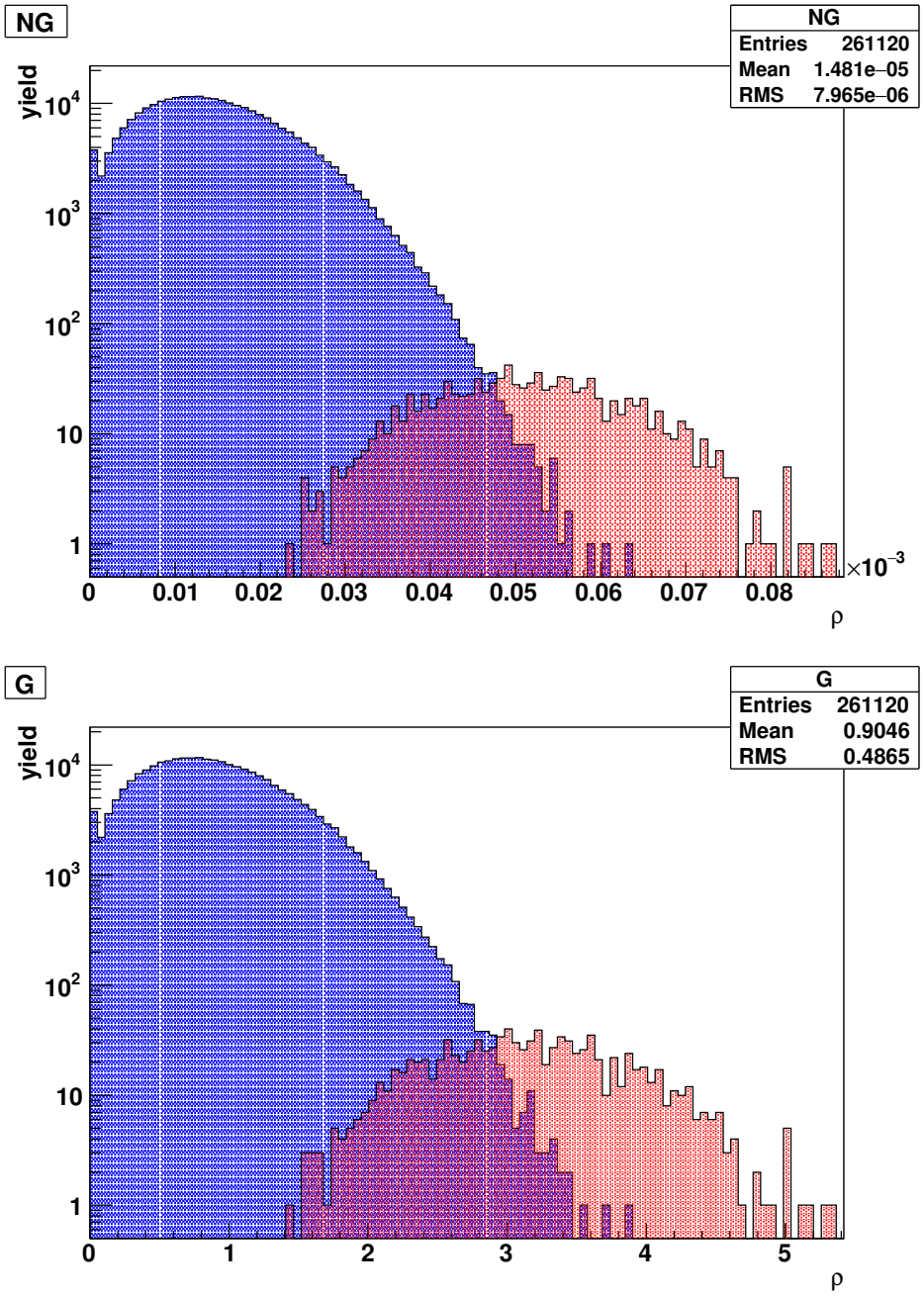

Figure 5.10: The histogram of $\hat{\rho}(t)$ of the Student-t filter(top panel) and the Gaussian matched filter(bottom panel) in the case of Student-t noise whose ν equal 25. The blue and red histogram in the both panel represent the $\hat{\rho}(t)$ of the background noise and the injected gravitational wave signal from binary coalescence event whose two masses and expected signal-to-noise ratio are $38.8M_{\odot}$, $31.6M_{\odot}$, and 3, respectively.

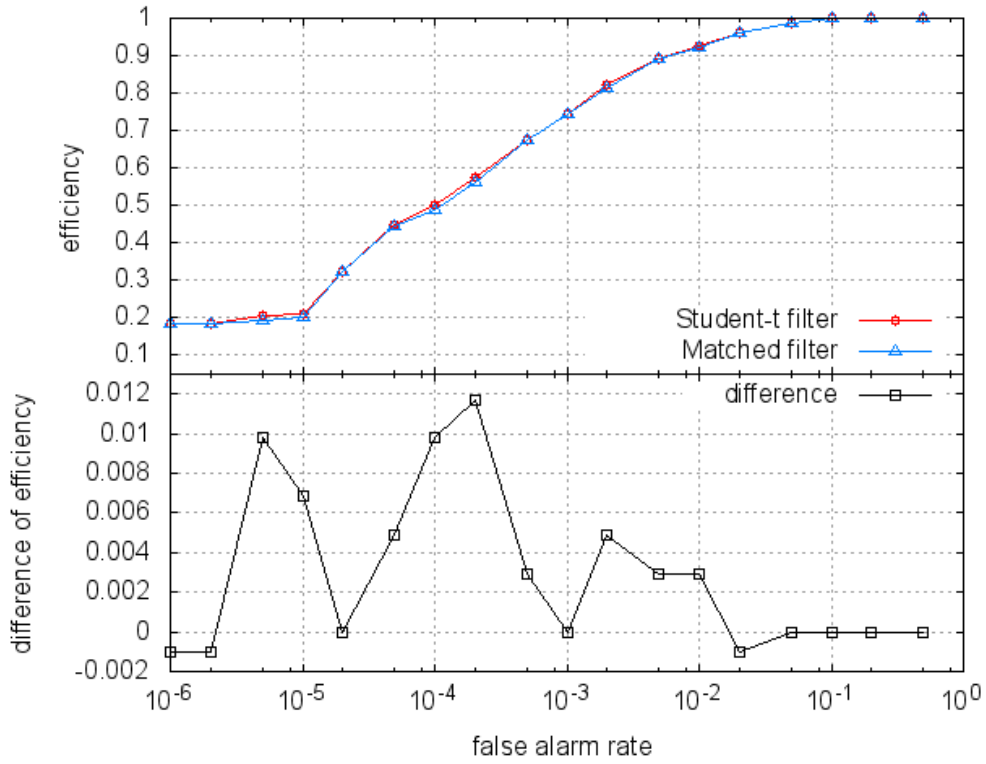

Figure 5.11: The histogram of difference between the $\hat{\rho}_{\mathrm{ST}}$ and $\hat{\rho}_{\mathrm{G}}$. The blue and red histogram represent the $\hat{\rho}$ of the background noise and the injected gravitational wave event.

5.2.3 GW150914

The optimal filter for the Student-t noise applied to the detector signal around GW150914 and output of optimal filter is shown in FIG. 5.12.

FIG. 5.12 shows the time series of optimal filter output for the detector data of LIGO at Hanford(top panel) and at Livingston(bottom panel) The template waveform is 3.5 PN order.

According to [60], the strain amplitude of GW150914 is maximum at 2048.39s of the axis label of 5.12. The time when the $\rho(t)$ is maximum is 2048.383606s.

The gravitational wave waveform of post-Newtonian is less accurate than the numerical relativity waveform which is used by advanced LIGO search especially around coalescence time. The results of $\rho(t)$ for various post-Newtonian order are shown in FIG. 5.13. The red, green, blue, pink, light blue, and yellow points represent $\rho(t)$ of Hanford LIGO data with the 1.0, 1.5, 2.0, 2.5, 3.0, and 3.5 post-Newtonian waveform, respectively. The x axis represents the elapsed time from 2048s of the FIG. 5.12.

The coalescence time t_c differs about 0.05s with different post-Newtonian order of the waveform. Our optimal filter can detect the GW150914 event at the correct time within the accuracy of the post-Newtonian waveform.

The statistical significance, $\hat{\rho}$, of the GW150914 can be estimated from the mean, μ_ρ, and standard deviation, σ_ρ, of the $\rho(t)$ when the gravitational wave

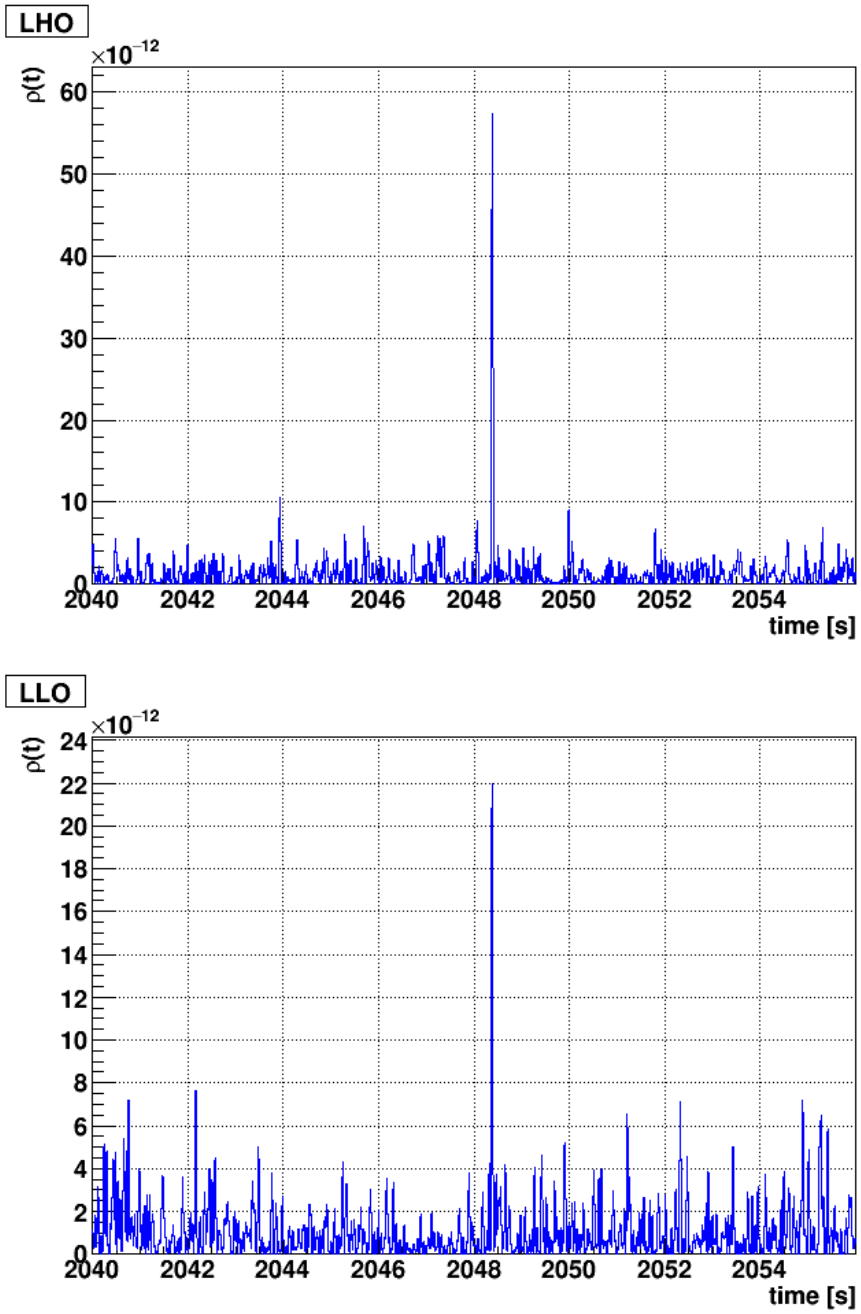

Figure 5.12: This plot shows the time series of the optimal filer output $\rho(t)$ with the Hanford LIGO(top panel) and the Livingston LIGO(bottom panel) of data around the GW150914.

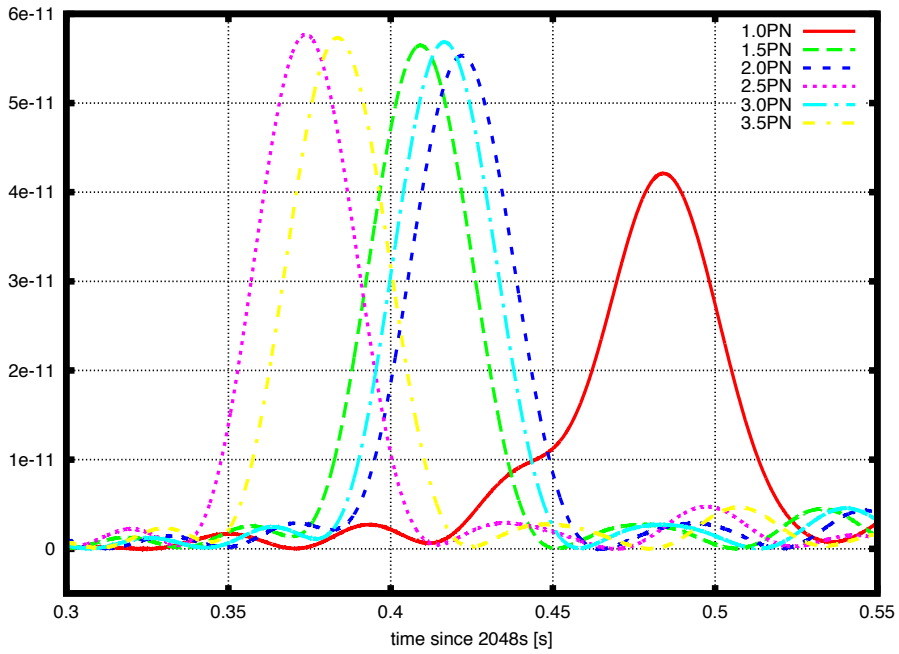

Figure 5.13: This plot shows the $\rho(t)$ of the data of Hanford LIGO around the coalescence time t_c with the various post-Newtonian waveform. The red, green, blue pink, light blue, and yellow points represent the $\rho(t)$ with the 1.0, 1.5, 2.0, 2.5, 3.0 and 3.5 post-Newtonian waveform, respectively.

Table 5.1: The mean and standard deviation of the $\rho(t)$

	Hanford	Livingston
$\mu_{\rho,ST}$	1.235e-12	1.069e-12
$\sigma_{\rho,ST}$	1.646e-24	1.333e-24
$\hat{\rho}_{\mathrm{ST}}(t)$	43.726	18.101
$\mu_{\rho,G}$	9.710e-13	9.188e-13
$\sigma_{\rho,G}$	9.955e-25	9.692e-25
$\hat{\rho}_{\mathrm{G}}(t)$	43.720	18.155

is absence. The $\hat{\rho}$ is defined as

$$\hat{\rho}_i = \frac{\rho_{\mathrm{GW150914,i}} - \mu_{\rho,i}}{\sigma_{\rho,i}}, \tag{5.11}$$

where i represents the Gaussian(G) or Student-t(ST) model. We regard the detector output of the LIGO data excluding 1 second around the time occurring GW150914 as the data in which the gravitational wave is absence.

There are no promising difference between the matched filter method and Student-t filter because the ν is not large enough for rejecting Gaussian assumption around the time and frequency of GW150914 and the signal-to-noise ratio of GW150914 is large.

Table. 5.1 shows the μ_ρ, σ_ρ, and $\hat{\rho}$. Our filter which is optimized for Student-t noise can detect the GW150914 with the 43.7σ(Hanford) and 18.1σ(Livingston) of the statistical significance.

Chapter 6

Conclusion

We proposed a method to characterize the non-Gaussianity of GW detector noise. Namely, we introduce Student-Rayleigh distribution to characterize possible non-Gaussianity of data. Here, the degrees of freedom ν of the distribution is found to be useful to quantify degree of non-Gaussianity. We use ν as a characteristic parameter, that represents weight of tail of detector noise. We calculated confidence interval of ν and threshold below which we reject the Gaussian hypothesis. We characterize the non-Gaussianity in realistic detector noise quantitatively.

The existence of non-Gaussian noise component in realistic detector noise is also clarified by our method with threshold and confidence interval. The threshold for rejecting Gaussian noise is evaluated for various data length T. In the case of $T = 4096$s and $\hat{\nu} = 25$, the 99% confidence interval is $15.45 < \nu < 27.29$.

In this work, we show the detection method for non-Gaussian noise using ν and the accuracy of ν. This method revealed continuous and transient non-Gaussian components in the LIGO data, by estimating the degree of non-Gaussianity of the detector noise every 16Hz and 1024s.

The degree of non-Gaussianity is related with the origin of noise source. The characteristics of non-Gaussianity, such as power, frequency and/or time evolution, are also different among noises of different origins, as shown in the spectrogram Fig. 9. Robustness for outliers derived from non-stationary noise of our method can be adjusted by changing quantile and p. The method using quantile is more robust for outlier than the one using the whole of the noise distribution such as χ^2-fitting.

Our method can be used for revealing stationary feature of the detector noise. So ν can provide information of noise status which is different from the one provided by the methods for non-stationary noise. When all deviations from Gaussianity are regarded as non-stationarity, it is difficult to identify mechanisms that cause stationary but non-Gaussian noises. Our method and methods for investigating transient noise are complementary to each other for evaluating conditions of the detector noise because our method can investigate stationary non-Gaussianity of detector noise. Regarding search for GWs we adopt the Student-t likelihood function as the optimal filter for Student-t noise model instead of matched filtering method. Student-t likelihood function is determined with a parameter ν which is estimated from the detector signals.

The Student-t filter is applied for simulated Gaussian noise, simulated Student-t noise, and the LIGO observational signal around GW150914. We compared output of Student-t filter with one of Matched filter. The difference of the output of the Student-t filter and Matched filter for Gaussian noise are the same within $3.83 \times 10^{-5}\sigma$. For the stationary Student-t noise, the ROC curve of the Student-t filter has improved 1% compared to that of matched filter at 10^{-4}-false alarm probability. The Student-t filter is provide a significance equivalent to the matched filter result for the GW150914 event though the non-Gaussianity of the detector noise around the GW150914 event is not dominant enough. We conclude that the Student-t filter can be used as a search method instead of the matched filter even though the detector noise is Gaussian noise.

Bibliography

[1] A. Einstein, Ann. Phys. (Berlin), **354** 769 (1916)

[2] R. A. Hulse and J. H. Taylor, Astrophys. J., **195** L51 (1975)

[3] J. H. Taylor and J. M. Weisberg, Astrophys. J., **345** 434 (1989)

[4] B. P. Abbott, et. al., Rep. Prog. Phys. **72** 076901 (2009)

[5] T. Accadia, et. al., JINST **7** P03012 (2012)

[6] J. Aasi, et. al., Phys. Rev. D **89**, 122003 (2014)

[7] J. Aasi, et. al., Phys. Rev. Lett. **113**, 231101 (2014)

[8] J. Aasi, et. al., Phys. Rev. D **91**, 062008 (2015)

[9] J. Abadie, et. al., Phys. Rev. D **85** 122007 (2012)

[10] M. A. Bizouard and M. A. Papa, C. R. Physique **14** 352-365 (2013)

[11] B. Abbott, et. al., Phys. Rev. D **77** 062004 (2008)

[12] J. Abadie, et. al., Astrophys. J. Lett. **734** L35 (2011)

[13] Gregory M. Harry and LIGO Scientific Collaboration, Class. Quantum Grav. **27** 084006 (2010)

[14] B. P. Abbott, et. al., Phys. Rev. Lett. **116** 061102 (2016)

[15] B. P. Abbott, et. al., Astrophys. J. Lett. **818** L22 (2016)

[16] F. Acernese, et. al., Class. Quantum Grav. **32** 024001 (2015)

[17] K. Kuroda, et. al., Class. Quantum Grav. **27** 084004 (2010)

[18] M. Ohashi, et. al., Class. Quantum Grav. **20** S599 (2003)

[19] T. Uchiyama, et. al., Phys. Rev. Lett. **108** 141101 (2012)

[20] M. Maggiore, "Gravitational Waves", Oxford University Press Inc., New York, (2008)

[21] P. Ajith, et. al., Phys. Rev. D **77** 104017 (2008)

[22] E. Müller, Class. Quantum Grav. **14**, 1445 (1997)

[23] J. Aasi et al., Phys. Rev. D **91** 022004 (2015)

[24] W. G. Anderson, et. al., Phys. Rev. D **60** 102001 (1999)

[25] W. G. Anderson, et. al., Phys. Rev. D **63** 042003 (2001)

[26] The KAGRA Collaboration,
URL: http://gwcenter.icrr.u-tokyo.ac.jp

[27] The KAGRA Collaboration,

URL: http://gwwiki.icrr.u-tokyo.ac.jp/JGWwiki/KAGRA

[28] The LIGO Collaboration,

URL: https://www.ligo.caltech.edu

[29] The LIGO Collaboration, LIGO-T0900288 (2010)

URL: https://dcc.ligo.org/cgi-bin/DocDB/ShowDocument?docid=2974

[30] The Virgo Collaboration,

URL: http://www.ego-gw.it

[31] The Virgo Collaboration, VIR-0128A-12 (2012)

URL: https://tds.ego-gw.it/itf/tds/file.php?callFile=VIR-0128A-12.pdf

[32] A. Araya, et. al., Rev. Sci. Instrum. **64** 1337 (1993)

[33] P. R. Saulson, "Fundamental of Interferometric gravitational wave detector", World Scientific (1994)

[34] P. R. Saulson, Phys. Rev. D **42** 2437 (1990)

[35] F. Bondu, et. al., Phys Lett A **246** 227 (1998)

[36] P. Jaranowski and A. Królak, Living Rev. Rel. **15** 4 (2012)

[37] J. Aasi, et. al., Class. Quantum Grav. **29** 155002 (2012)

[38] Jessica McIver, Class. Quantum Grav. **29** 124010 (2012)

[39] LIGO Scientific Collaboration, "LIGO Open Science Center release of S5", 2014, DOI 10.7935/K5WD3XHR

[40] M. Vallisneri, et. al., J. Phys. Conf. Ser. **610** 012021 (2015)

[41] J. Aasi, et.al., Class. Quantum Grav. **32** 115012 (2015)

[42] J. R. Smith, et. al., Class. Quantum Grav. **28**, 235005 (2011)

[43] Parameswaran Ajith, et. al, Phys. Rev. D **89**, 122001 (2014)

[44] N. Christensen for the LIGO and VIRGO Scientific Collaboration, Class. Quantum Grav. **27** 194010 (2010)

[45] J. Slutsky et. al., Class. Quantum Grav. **27** 165023 (2010)

[46] Michael Coughlin, 2010 J. Phys.: Conf. Ser. **243** 012010 (2010)

[47] Michael W. Coughlin, Class. Quantum Grav. **28** 235008 (2011)

[48] J. D. Creighton, Phys. Rev. D **60**, 021101 (1999)

[49] B. Allen, J. D. Creighton, E. E. Flanagan and J. D. Romano, Phys. Rev. D **65**, 122002 (2002)

[50] C. Röver, Phys. Rev. D **84**, 122004 (2011)

[51] R. Biswas, et. al., Phys. Rev. D **85** 122009 (2012)

[52] M. Principe and I. M. Pinto, Class. Quantum Grav. **26** 204001 (2009)

[53] Student, Biometrika **6**, 1, 1-25 (1908)

[54] C. Röver, R. Meyer and N. Christensen, Class. Quantum Grav. **28**, 015010 (2011)

[55] C. Röver, LIGO Document, LIGO-T1100497-v1 (2011) URL: https://dcc.ligo.org/LIGO-T1100497/public

[56] Kenneth L. Lange, et.al., Journal of the American Statistical Association **84**, 881-896 (1989)

[57] B. P. Abbott, et. al., Phys. Rev. D **80**, 102001 (2009)

[58] James E. Gentle, "Elements of Computational Statistics", Springer-Verlag New York (2002)

[59] Jolien D. E. Creighton, et. al., WILEY-VCH Verlag GmbH & Co. KGaA, Boschstr. 12, 69469 (2012)

[60] LIGO Scientific Collaboration, "LIGO Open Science Center release of GW150914", 2016, DOI 10.7935/K5MW2F23

Acknowledgment

I would like to really appreciate to Prof. N. Kanda for introducing me to the gravitational wave experiment physics and for giving me many suggestions for gravitational wave analysis. I would like to be grateful to Dr. K. Hayama for introducing me to the subject related to the detector characterization and for continuous support. I would like to thank to Prof. S. Mano and Dr. Y. Itoh for instructive discussions and helpful comments. I would like to thank to Prof. H. Tagoshi, Dr. T. Yokozawa, Dr. T. Narikawa, Dr. K. Ueno, Dr. M. Kaneyama H. Yuzurihara, K. Tanaka, A. Miyamoto, Y. Okada, M. Asano, and M. Toritani for very useful discussions. Finally, I would like to express my gratitude to my family.

This research has made use of data, software and/or web tools obtained from the LIGO Open Science Center (https://losc.ligo.org), a service of LIGO Laboratory and the LIGO Scientific Collaboration. LIGO is funded by the United States National Science Foundation. This work was supported by MEXT Grant-in-Aid for Scientific Research on Innovative Areas "New Developments in Astrophysics Through Multi-Messenger Observations of Gravi-

tational Wave Sources" (Grant Number 24103005). This work was supported by JSPS Grant-in-Aid for Specially Promoted Research.